CZECH TECHNICAL UNIVERSITY IN PRAGUE
Faculty of Nuclear Sciences and Physical Engineering
Department of Physics

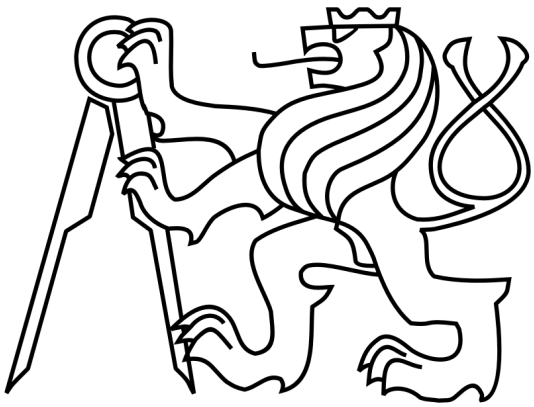

Research project

Eliptic flow of J/ψ meson in $U+U$ collisions at STAR experiment

Alena Harlenderová

Supervisor: RNDr. Petr Chaloupka, Ph.D.

Prague, 2016

ČESKÁ TECHNICKÁ UNIVERZITA V PRAZE
Fakulta jaderná a fyzikálně inženýrská
Katedra fyziky

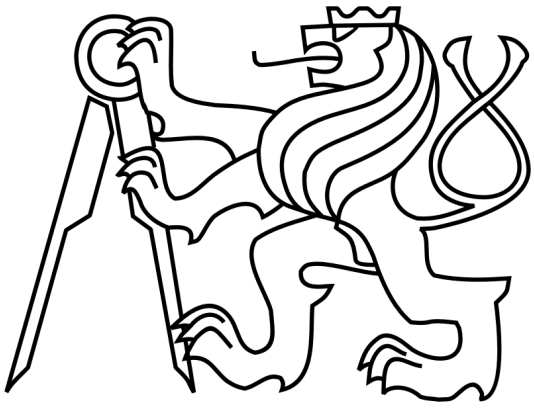

Výzkumný úkol

Eliptický tok mezonu J/ψ ve srážkách $U+U$ na experimentu STAR

Alena Harlenderová

Supervisor: RNDr. Petr Chaloupka, Ph.D.

Praha, 2016

ČESKÉ VYSOKÉ UČENÍ TECHNICKÉ V PRAZE
FAKULTA JADERNÁ A FYZIKÁLNĚ INŽENÝRSKÁ
PRAHA 1 - STARÉ MĚSTO, BŘEHOVÁ 7 - PSČ 115 19

Katedra: fyziky **Akademický rok:** 2015/2016

VÝZKUMNÝ ÚKOL

Posluchač: Bc. Alena Harlenderová

Obor: Experimentální jaderná a částicová fyzika

Vedoucí úkolu: RNDr. Petr Chaloupka, Ph.D., FJFI ČVUT

Název úkolu (česky/anglicky):

Eliptický tok J/ψ mesonu ve srážkách U+U na experimentu STAR
J/ψ elliptic flow in U+U collisions at the STAR experiment

Pokyny pro vypracování:

1. Seznámení se s fyzikou srážek ultrarelativistických těžkých jader.
2. Studium problematiky produkce těžkých kvarkonií se zaměřením na eliptický tok pozorovaných částic.
3. Analýzy dat experimentu STAR ze srážek jader uranu nabraných v roce 2012 při těžišťové energii $\sqrt{s_{NN}}$= 200 GeV.
4. Analýza eliptického toku v_2 J/ψ mesonu zrekonstruovaného z rozpadového kanálu e^+e^-.

Součástí zadání výzkumného úkolu je jeho uložení na webové stránky katedry fyziky.

Literatura:

[1] J. Adams et al.; Nucl. Phys. A757, 102 (2005), nucl-ex/0501009.
[2] T. Matsui and H. Satz; Physics Letters B 178, 416 (1986).
[3] S. Gavin, M. Gyulassy, and A. Jackson; Physics Letters B 207(3), 257–262, 1988,
[4] P. Braun-Munzinger and J. Stachel, Phys. Lett. B490, 196 (2000), nucl-th/0007059.
[5] D. Kikola, G. Odyniec, and R. Vogt; Phys. Rev. C84, 054907, 2011
[6] A. Frawley, T. Ullrich, and R. Vogt; Phys. Rept. 462, 125–175, 2008
[7] B. I. Abelev, et al.; Phys. Rev. C 80, 041902
[8] L. Adamczyk, et al.; ArXiv:1507.05247
[9] L. Adamczyk, et al.; Phys. Rev. Lett. **111** (2013) 52301

Datum zadání: 23.10.2015 .....

Datum odevzdání: 24.06.2016 ***vedoucí katedry***

Prohlášení

Prohlašuji, že jsem svůj výzkumný úkol vypracovala samostatně a použila jsem pouze podklady (literaturu, software, atd.) uveřejněné v přiloženém seznamu.

Nemám závažný důvod proti užití tohoto školního díla ve smyslu §60 Zákona č.121/2000 Sb., o právu autorském, o právech souvisejících s právem autorským a o změně některých zákonů (autorský zákon).

V Praze dne 23.6.2016

Title:
Eliptic flow of J/ψ meson in $U+U$ collisions at STAR experiment

Author: Alena Harlenderová

Specialization: Experimental nuclear and particle physics

Sort of project: Research project

Supervisor: RNDr. Petr Chaloupka, Ph.D.

Abstract: The analysis of the azimutal anisotropy in non-central collisions is one of the most important instruments for studying properties of matter created in heavy ion collisions. The azimutal distribution (anistrophic flow) of particle momentum is expected to be sensitive to early stages of the collision. Studying J/ψ eliptic flow can shed more light on the production of J/ψ and interaction of J/ψ with the hot deconfined medium. First steps to v_2 J/ψ calculation from U+U data were performed and are presented in this research task. Event plane azimuthal angles were corrected on TPC efficiency. Electrons and positrons were preselected and unlike-sign and like sign-pairs were saved in PicoDsts. J/ψ signal from events triggered as central, minimum bias or with hit in high tower was reconstructed. Further steps of v_2-calculation procedure are going to be discussed.

Key words: Eliptic flow, azimuthal anisotropy, meson *Jpsi*, ultrarelativistic heavy ion collisions.

Název práce:
Eliptický tok mezonu J/ψ ve srážkách $U + U$ na experimentu STAR

Autor: Alena Harlenderová

Zaměření: Experimentální jaderná a částicová fyzika

Typ práce: Výzkumný úkol

Supervisor: RNDr. Petr Chaloupka, Ph. D.

Abstrakt: Analýza azimutální anizotropie v necentrálních ultrarelativistických srážkách těžkých iontů je jeden z nejdůležitějších nástrojů pro studium hmoty v těchto srážkách. Předpokládá se, že je azimutální rozdělení (anizotropický tok) hybnosti částic citlivé na počáteční stádia srážek. Studium eliptického toku mezonu J/ψ může pomoci objasnit produkční mechanismus J/ψ a osvětlit způsob interakce J/ψ s horkým médiem. Byly učiněny první kroky k výpočtu v_2 J/ψ ze srážek U+U provedených na experimentu STAR. Byl proveden recentering azimutálního úhlu event plane. Elektrony a pozitrony byly předvybrány. e^+e^-, e^-e^- and e^+e^+ páry byly uložený uloženy do PicoDst. Signál J/ψ z centrálních srážek, minimum bias srážek a srážek s elektronem s vysokou hybností byl rekonstruován přes dielektronový rozpadový kanál. Další kroky pro výpočet v_2 jsou diskutovány ve výzkumném úkolu.

Klíčová slova: Eliptický tok, azimutální anizotropie, mezon J/ψ, ultrarelativistické srážky těžkých iontů, event plane.

Acknowledgement

I would like to thank RNDr. Petr Chaloupka, Ph.D. for his patience, inspiring consultations and his help in the beginnings that are always hard.

Contents

Introduction

The analysis of the azimutal anisotropy in non-central collisions is one of the most important instruments for studying properties of matter created in heavy ion collisions. The azimutal distribution of particle momentum is expected to be sensitive to early stages of the collision. The azimuthal part of momentum distribution can be decomposed by using the Furier transform. The second Fourier coefficient v_2 is called elliptic flow. Studying J/ψ eliptic flow can shed more light on the production of J/ψ and interaction of J/ψ with the hot deconfined medium.

First steps to v_2 J/ψ calculation from U+U data were performed and are presented in this research task. TPC does not have azimuthally uniform efficiency, thus event plane azimuthal angles are corrected on TPC efficiency by method called recentering. Afterwards, corrected event plane azimuthal angles are calculated.

Electrons and positrons are preselected and unlike-sign and like-sign pairs are saved in smaller files called PicoDsts, since running code on PicoDsts is faster. J/ψ signal from events triggered as central, minimum bias or with hit in high tower was reconstructed via dielectron decay channel for following J/ψ transverse momenta bins: $0 < p_T < 2\text{GeVc}^{-1}$,$2 < p_T < 5\text{GeVc}^{-1}$, $5 < p_T < 20\text{GeVc}^{-1}$. Further steps of v_2 calculation procedure are discussed. Theoretical grounds of invariant mass method and event plane method are explained.

Ultrarelativistic heavy ion collisions and hot dense medium created in them are described in the first chapter. Second chapter is dedicated to the STAR experiment, which recorded data from $U + U$ collisions. Afterwards, eliptic flow and its importance is decribed in the third chapter. Part of STAR results on v_2 of hadrons and J/ψ meson is shown. Hadrons composed of light and strange hadrons have significant eliptic flow, whereas results on eliptic flow of J/ψ in Au+Au collisions are consistent with zero from $p_T \approx 2\text{GeVc}^{-1}$. Finally, performed data analysis is presented in the last chapter.

Chapter 1

Ultrarelativisic Heavy Ion Collisions

Heavy ions can be accelerated to the very high energies. Afterwards, they can be collided with static target or between themselves. If the energy density of $\epsilon \approx 1\text{GeV/fm}^3$ is reached during heavy ion collision, we call it ultrarelativistic [**19**]. This energy can be reached and surmounted at heavy ion colliders such as the Large Hadron Collider LHC or Relativistic Heavy Ion Collider (RHIC).

The capability of reaching such energies is a great opportunity for studying strongly interacting matter under extreme conditions. It is believed that the energy densities reached at mentioned colliders are high enough for a creation of other stage of matter, a quark-gluon plasma (QGP).

At first, the properties of strongly interacting matter are going to be described. Afterwards, the space-time evolution of an ultrarelativistic heavy ion collision will be discussed.

1.1 Properties of strongly interacting matter

1.1.1 Colour confinement and asymptitic freedom

Every quark and gluon has quantum number called colour. It is similar to the role of + and − charge in the case of electromagnetic interaction. Similarly as we get zero charge if we put together + and −, we gain colourless white if we mix together red, green and blue. Additionally, there are anticolours carried by antiquarks and gluons: antired, antiblue and antigreen. The colour with its anticolour create together also colourless state. Quarks and antiquarks that are together colourless can be bound in hadrons. If there are two quarks in hadron, we call it meson, in the case of three baryon. Quarks are bounded in hadrons by the strong interaction, which is described within theory called quantum chromodynamics (QCD).

The binding of quarks can be for simplicity explained on the example of the Cornell quark-antiquark potential [**20**]:

$$V(r) = -\frac{4}{3}\frac{\kappa}{r} + kr, \tag{1.1}$$

where r is distance between quark and antiquark, κ constant and k the string tension potential.

The second part of the Cornell potential is called string potential. It manifests itself at higher distances r by strong attraction of quark and antiquark. If quark and antiquark move away from each other, energy of the potential rises. If it exceeds a mass of quark and its antiquark, new quark-antiquark pair is created. Thus, quarks and antiquarks can not be simply separated from each other. They are bounded in colourless hadrons at lower temperatures and baryon chemical potentials. This phenomenon is called colour confinement [**21**].

The Coulomb-like part of the potential, is significant at lower distances, whereas influence of the other part of potential weakens. Thus, quarks and antiquarks behave like almost free in very dense matter in comparison to long distances. This phenomenon is called asymptotic freedom [**19**]. Similar behaviour can be observed also for high temperatures.

1.1.2 Quark-Gluon plasma

QCD predicts the phase transition between hadronic matter and quark-gluon plasma (QGP) at high temperatures [**25**]. Hadrons are deconfined, quarks as new degrees of freedom are liberated and are assymptotically free. This stage of matter and phase transition is the object of intensive research. The Beam Energy Scan I performed at RHIC confirmed the evidence for the quark-gluon plasma QGP discovery at the center of mass energy $s_{NN} = 200\text{GeV}$ [**25**].

Possible QCD phase diagram with the baryon chemical potential μ_B on the horizontal axis and the temperature T on the vertical axis can be seen in the Figure 1.1. Nuclear matter is characterized with approximately zero temperature and baryon chemical potential around 900MeV. If the temperature increases and baryon chemical potential is not close to zero, the hadronic stage of matter changes by the first order phase transition to QGP. Smoother phase quark-hadron transition of second order called crossover is predicted for zero baryon chemical potential by the lattice QCD [**25**]. The point between crossover and the first order transition is named critical point.

If baryon chemical potential increases and temperature is near to zero, matter gets to colour-superconductivity stage. It is supposed that this stage of matter is present in neutron stars.

1.2 Space-time evolution of a heavy-ion collision

The colliding of heavy ions at ultrarelativistic energies is the way to explore propeties of strongly interacting matter under extreme conditions such as high

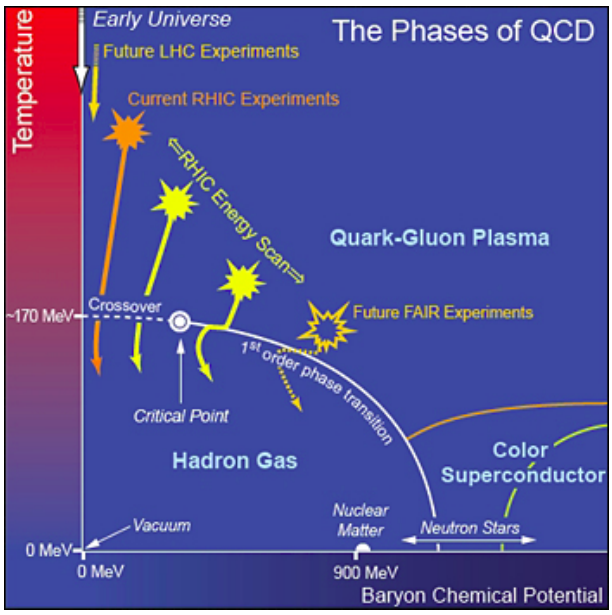

Figure 1.1: Schematic QCD phase diagram for nuclear matter with the baryon chemical potential μ_B on the horizontal axis and the temperature T on the vertical axis. The solid lines represent phase transitions of the first order, dashed line crossover. The picture is taken from [**25**].

temperature and high energy density. Whole space-time evolution of a ultrarelativistic heavy ion collision can be seen in the Figure 1.2. Individual evolution phases of these collisions are going to be briefly discussed in this subchapter [**19**].

- Partons in heavy ions hardly scatter of each other in the beginning of a collision. Extensive amount of energy is released and new quark and gluons are created. The amount of released energy is suffices to a creation of heavy quarks.
- The system thermalizes briefly in the proper time $\tau \leq 1\text{fm/c}$ and a thermal equilibrium is established. Quarks and gluons are asymptotically free in the QGP phase. Particles behave collectively and collided nuclei can be considered as a system, not collection of particles. This phase can be described by an equation of state.
- System further expands and cools down. If temperature reaches critical temperature of $T_c = 170\text{MeV}$, phase transition takes place. Quarks cease to be asymptotically free and commence to be bound in hadrons again.
- Medium expands further and get to the temperature of chemical freeze-out T_{ch}. The composition of hadrons does not change any more. However, they collide elastically.
- If the temperature of kinetic freeze-out T_{fo} is reached, hadrons cease to interact between themselves. They just fly away from a place of collision and can be detected by experimental setup.

Unfortunately, described evolution can not be observed directly. We are able to observe only the result of collision in a form of escaping particles.

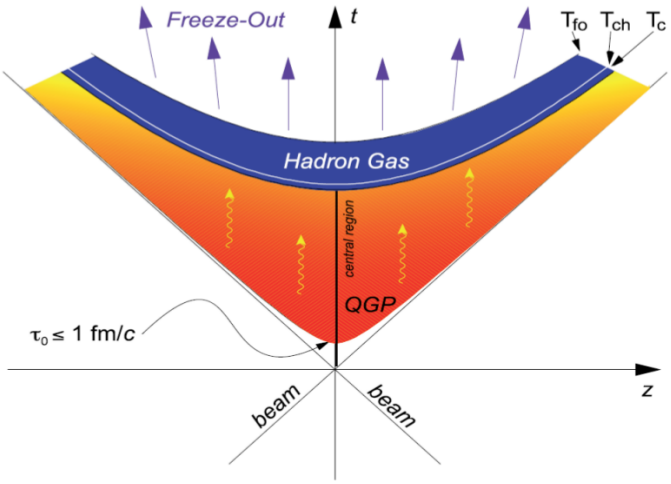

Figure 1.2: Evolution of a central ultrarelativistic heavy-ion collision. The picture is taken from [**19**].

Chapter 2

Experimental Setup

2.1 Relativistic Heavy Ion Collider

The Relativistic Heavy Ion Collider (RHIC) is situated in the Brookhaven National Laboratory near New York. RHIC is unique device capable of acceleration and colliding broad pallet of heavy ions and protons among themselves at various energies. Moreover, it is the only machine that can collide high-energy beams of polarized protons [**1**].

The RHIC complex can be seen in the Figure 2.1. Atoms are ionized and firstly accelerated in the Electron Beam Ion Source (EBIS), which is able to inject ions of stable elements from deuterium to uranium. Similar role for protons performs the Linear Accelerator (Linac). Afterwards, protons and ions travel to Alternating Gradient Synchrotron (AGS) Booster and are further accelerated. Finally they are injected into RHIC, where they are boosted to full energy of light. Beams in RHIC run in oposite directions in two hexagon-shaped storige rings, which intersect at six points. There are two experiments, the Solenoidal Tracker At RHIC (STAR) and the Pioneering High Energy Nuclear Intersection eXperiment (PHENIX), at intersect poins. Particles created in collisions are detected by complex systems of detectors at these points.

The first run, in which ^{197}Au+^{197}Au were collided at the center of mass energies per nucleon-nucleon pair $s_{NN} = 55.8$GeV took place in 2000 [**2**]. Following collisions were performed since this time: Au+Au collisions at total energy per nucleon from 3.85GeV to 100GeV , Cu+Cu from 11.2GeV to 100GeV, U+U collisions at 96.4GeV, Cu+Au at 99.9 + 100GeV, d+Au from 9.8GeV to 100.7 + 100GeV, h+Au at 103.9 + 100GeV, p+Au at 103.4 + 97.4, p+Al at 103.4 + 98.6GeV and collisions of two polarized protons from 21.2GeV to 254.9GeV [**2**].

We will be interested in $U+U$ collissions at total energy per nucleon 96.4GeV (corresponding to $s_{NN} = 192.8$GeV), because the analysis of the data from these collisions is presented in this research project.

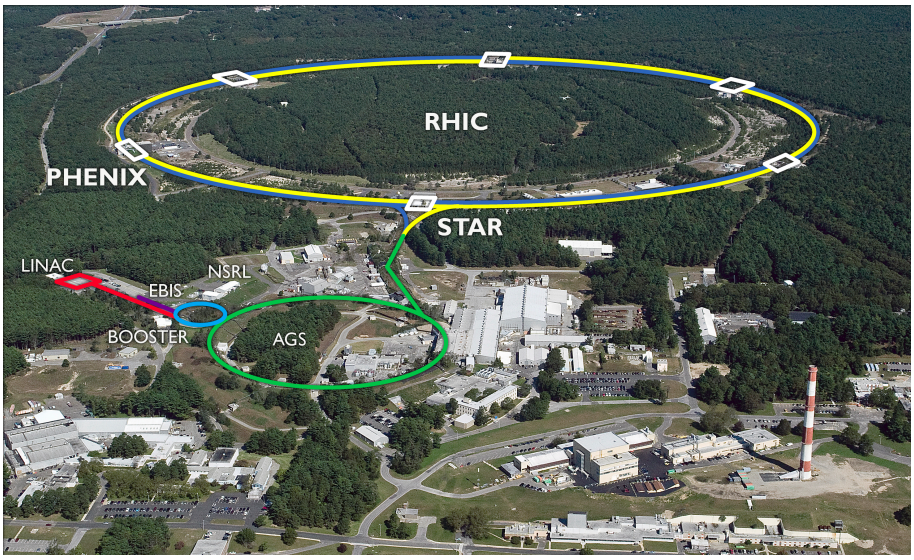

Figure 2.1: The complex of RHIC. LINAC (red colour) inject and firstly boosts protons, whereas EBIS (violet) ions. Ions are further accelerated in AGS (green) and their travel ends in RHIC storige rings (blue and yellow). The picture is taken from [**28**].

2.2 STAR Experiment

STAR detector focuses on exploring properties of strongly interacting matter at high temperatures and densities and phases of this matter, espetially QGP [**6**].

STAR is complex system of detectors. It covers azimuthal angle from 0 to 2π and track's particles with pseudorapidity $|\eta| < 1.8$ [**6**]. There are two main groups of the detectors, the detectors for the tracking and the identifying of particles and the triggers. The composition of the STAR detector with the names of the most important detectors can be seen in the Figure 2.2. The beam passes through the center of the detector. The Heavy Flavour Tracker (HFT) is situated in the proximity of the beam. If we move further away from the beam, the Time projection Champer (TPC), the Time Of Flight (TOF) and the Barrel ElecroMagnetic Calorimeter (BEMC) follow. They are surrounded by magnets, which prodice the uniform magnetic field around the beam with magnetic induction from $B = 0.25$T to $B = 0.5$T [**7**]. There is the Muon Telescope Detector (MTD) placed around the magnets. There are also detectores placed near to the beam from few meters to approximately 20 meters away from interaction point. The Beam Beam Counters (BBCs) are situated 3.5m from the interaction point at both sides of before mentioned detectors. The STAR Endcap Electromagnetic Calorimeters (EEMCs), the Vertex Position Detectors (VPDs) and the Zero Degree Calorimeters (ZDCs) are placed in a larger distance from the interaction point near to the beam.

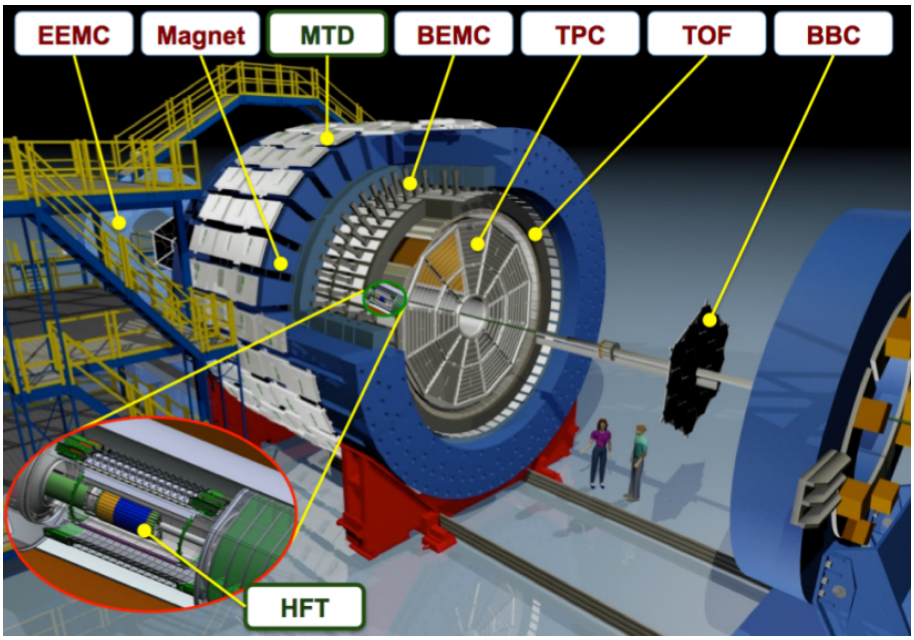

Figure 2.2: The picture of STAR experiment with names and positions of few main detectors. The picture is taken from [**4**].

The most important detectors are going to be described in this reserch task. The STAR triggering system will be also discussed.

2.2.1 The Time Projection Chamber

The Time Projection Chamber is located between the Heavy Flavour Tracker and the Barell Electromagnetic Calorimeter. The main purposes of TPC are is to track charged particles and identify them via their specific energy loss.

The design of TPC can be seen in the Figure 2.3. TPC has cylindrical shape. It is 4.2m long, outer and inner diameters are 4m and 0.5m [**24**]. TPC covers pseudorapidity $|\eta| < 1.8$ and the full azimuthal angle. It is divided to two hemispheres, the West and the East one, by the Central membrane. The membrane is held on the voltage -28kV [**24**]. The earthed ends are divided to 12 sectors and each of them is further split to 45 pad rows working as the Multi–Wire Proportional Chamber. They provide the readout.

It is filled with 10% of methan and 90% of argon. A pressure is held 2mb above the atmospheric pressure.

TPC is held in the homogenous magnetic field, therefore tracks of particles in TPC are curved to the shape of a helix. If the charged particle traverses this detector, it leaves ionized atoms and electrons along its track. Electrons travel to the caps, whereas ions to the Central membrane. The projection of a particle

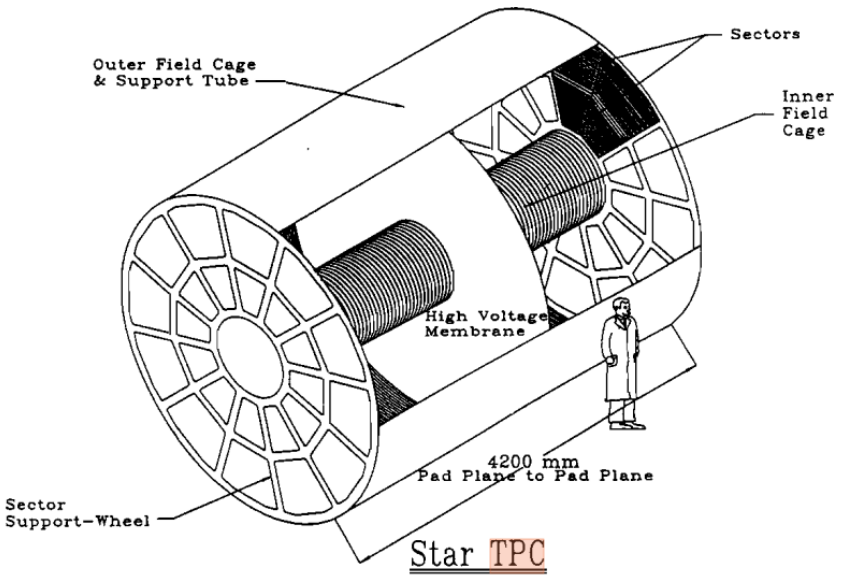

Figure 2.3: The design of the Time Projection Chamber. The Figure is taken from [**8**].

track to the x, y-plane in TPC is determined by the arrival place on the pad rows. We are also interested in z-position of a particle. It is obtained by the measurement of an arrival time of elecrons with respect to the collision time and dividing this time by the average drift velocity of electrons. If x, y-possition and z-position of track points are put together, the point is recunstructed. The absolute maximum number of hit points is 45 [**9**]. Nevertheless, the maximum of hit points for a concrete track depends on a presudorapidity, a particle momentum and a charge. The tracks are reconstructed by fitting the poins.

All tracks from one collisions are called the global tracks. If this collection is known, the primary vertex can be reconstructed. After that the distance of closes approach (DCA) of tracks to primary vertex is determined. If a DCA for a concrete particle track has the smaller DCA than 3 cm, it is considered to be the primary track [**9**]. The primary tracks are refitted with the use of the primary vertex point and all hits from TPC.

TPC is used also for particle identification as was mentioned earlier. Particles with the same ivariant mass and momentum have specific mean ionization energy loss in a defined medium. Ideally, particles lose energy according to their Bichsel functions. However, the measured ionization energy loss randomly fluctuates around this value. It can be seen in the Figure 2.4, where the Bichsel functions and the distribution of the energy loss recorded by TPC is shown.

A momentum of a particle can be obtained also with a help of TPC. Tracks are curved according to the Lorentz force and electric and magnetic induction

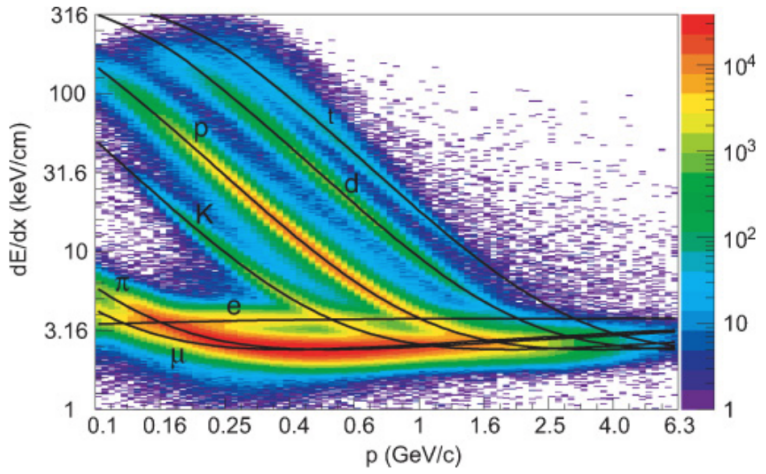

Figure 2.4: The distribution of the energy loss dE/dx of reconstructed tracks vs. particle momentum. The black lines are Bichsel functions for electrons, positrons, mions, charged pions, charged kaons, protons, deuterons and tritia. The Figure is taken from [**11**].

are known.

2.2.2 The Time of Flight

The Time of Flight Detector [**23**] is situated between TPC and the BEMC as can be seen in the Figure 2.2. As the name of the detector suggests its main purpose is measurement of particle's time of flight. A velocity and better particle identification is obtained with the help of informations from TOF and TPC.

The detector is divided to 120 segments, which together cover pseudorapidity $|\eta| < 1.0$. There are 32 chambers in the each segment. They contain resistive plates and between them are gaps filled with a gas. This tipe of the detector is called the Multigap Resistive Plate Chambers (MRPC). Electrodes are put on the the outer sides of the outer plates.

If particles traverse through the gas in TOF, they leave electrons and ionized atoms behind them. Electrons drift to the anode. Since, electric field is strong enough to speed up electrons to the velocity sufficient to the ionization of other atoms, other electrons are released and avelanches are created. The glass plate is polarized by arriving electrons and electrons on the other side of the plate are free to create an avalanche in the other gap. Finally, they are read out the arrival time t_1 is recorded.

However, it is needed to record starting time t_0 and to know time t_0 to t_1. t_0 is provided by the Vertex Position Detector (pVPV), whereas track is

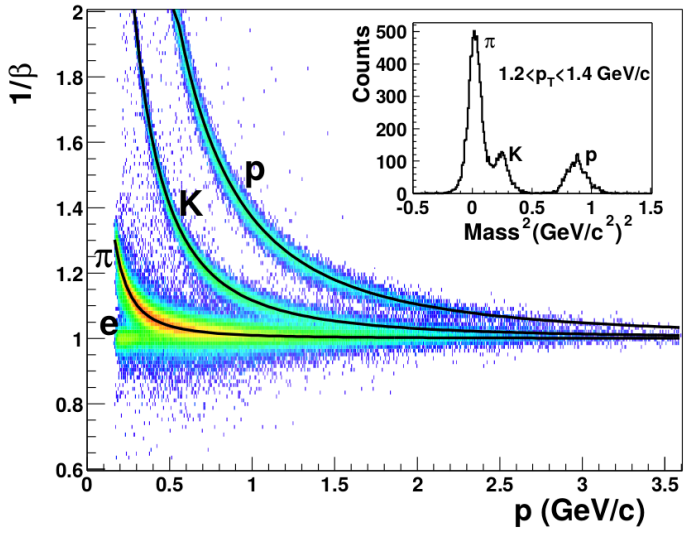

Figure 2.5: $1/\beta$ vs. momentum for $pi^{\pm}$, $K^{\pm}$ and $p^{\pm}$ from d+Au collisions at $\sqrt{s} = 200$GeV. The Figure is taken from [**22**].

reconstructed by TPC. Velocity β is obtained by the easy formula

$$\beta = \frac{\Delta s}{c(t_1 - t_2)}. \tag{2.1}$$

An invariant mass of a particle equals to

$$m_0 = \frac{p}{c}\sqrt{\frac{1}{\beta^2} - 1}, \tag{2.2}$$

where momentum p is from TPC. The distribution of the inverse velocity $1/\beta$ as the function of the momentum p is depicted in the Figure 2.5.

TOF is excellent tool for the identification of particles with lower p. For example, the identification of electrons up to $p = 1.4$GeV has good quality. For electrons with higher p also the BEMC signal is used for the identification.

2.2.3 The Barell Electromagnetic Calorimeter

The Barell Electromagnetic Calorimeter [**12**] is situated between TOF and magnets. Its main purpose is to distinguish electrons, positrons and gamma photons from hadrons and to measure energy of electrons.

BEMC covers full azimuthal angle and pseudorapidity $|\eta| < 1.0$. It is composed of 120 calorimeter moduls, which are devided to 40 towers. The core of the detector consists of 20 plates from lead and plates of a plastic scintilator as can be seen in the Figure 2.6. 19 scintilator layers and all lead layers are 5mm

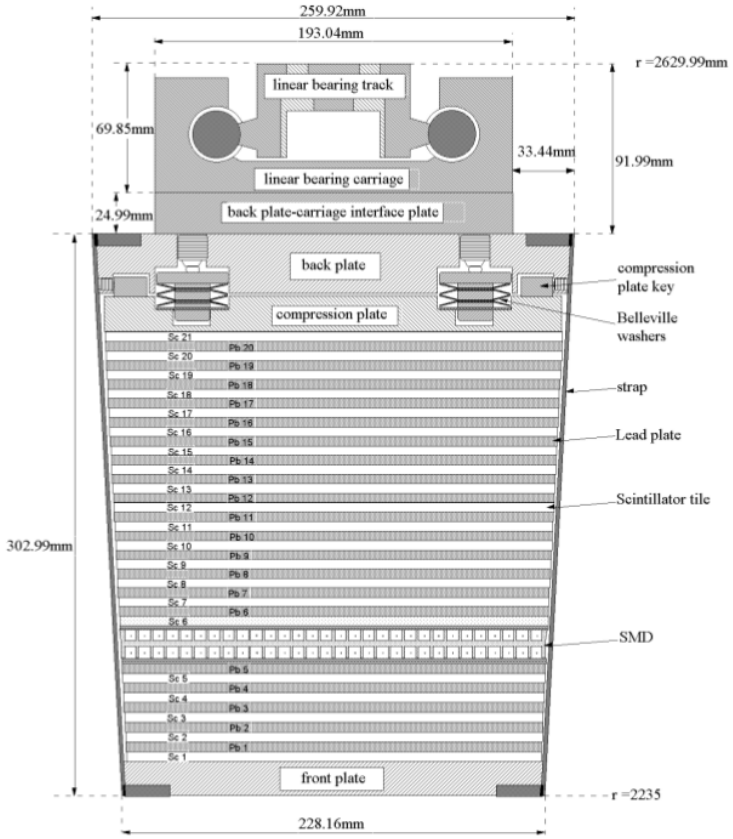

Figure 2.6: A module of the Barell Electromagnetic Calorimeter. The Figure is taken from [**11**].

thick, two of scintilators are 6mm thick. The Barrel Shower Maximum Detector (BSMD) is situated between the fifth layer of lead and the sixth layer of the scintilator. It is wire proportional counter with a gas amplification. The BSMD determines the 2D profile of showers in the place, where are suppoused to be broadest.

If an electron traverses the lead plate, it interacts electromagnetically and electromagnetic showers are created. Showers pass to the scintilator plates. Here the electrons from showers interact with the scintilator material and scintilation light is emmited. Electrons are supposed to lose all their energy by this way, whereas the interaction with hadrons is not so strong. Thus, the information from BEMC helps to distinguish between electrons and hadrons by this way. BEMC also provides the energy of the original electron.

2.2.4 Triggering system

All data from STAR detector can not be stored, thus triggers are used to commence storing data and choose events that will be stored. There are four levels of triggers. First three of them with levels L0,L1,L2 are detectors with a fast responce, for the last trigger level L3 is used information from slower detectors [**16**]. At L3 the final decision is made. The trigger detectors are for example:

- The Zero Degree Calorimeters [**17**] are placed 18.25m from the interaction point around beam pipe on the west and east side. They are hadronic calorimeters. Its main purpose is to measure spectator neutrons. Charged particles and between them also spectator protons are deflected in the magnetic field, whereas neutrons are not. They are deflected only less than 2mrad from the beam pipe. The coincidence between West and East ZDC is used as minimum bias trigger.

- Two Vertex Position Detectors (VPDs)[**18**] are placed 5.6m from the interaction point near to the beam pipe [**18**]. They are made of plastic scintilators and lead plates [**9**]. These detectors are built to measure arrival time of fotons from π^0 decays occuring at the primary vertex. The difference between arrival time of these photons is used to the calculation of the primary vertex possition. The average time is used as the start time for TOF. VPD serves also as L0 trigger because of its very fast response and as minimum bias trigger together with ZDCs.

- TOF is used as trigger of central collisions. More central collisions have higher multiplicity and it results in higher number of TOF hits. Thus, high number of hits in TOF is indicator of a central event.

- BEMC serves as trigger for events with hight-p_t processes such as jets or electrons from quarkonia di-electron decay channels. [**12**].

- MTD is used as trigger for di-muon events [**15**] and cosmic rays [**14**].

Chapter 3

Eliptic Flow

3.1 Non-central collisions and anisotrophic particle flow

The azimutal distribution (anistrophic flow) of produced particles is expected to be sensitive to early stages of a collision [**10**]. There is considerable azimutal anisotrophy in spatial distribution of matter in non-central collisions as can be seen in the Figure 3.1. The medium is in the shape of "almond" due to the initial geometry of the collision and is thermalized briefly after the collision. Initial azimuthal anisotrophy results in a preassure gradient which has different magnitude at different places of the transverse plane, as is depicted in the Figure 3.2. The thermalized medium expands and an expansion is faster in a direction of the largest gradient. In the other words, particles are in average more accelerated in this direction and have significant values of a transverse momentum p_T. Overall, the initial azimuthal anisotrophy in distribution of matter results in the anisotrophy in the azimuthal distribution of momentum of emitted particles.

A direction of an azimuthal flow depens on a azimuthal direction of an almond. It is determined by reaction plane defined as a plane containing centres of nuclei and beam directions as is shown in the Figure 3.1. However, a reaction plane is not direct observable. A position of a reaction plane can be estimated by an azimuthal flow itself. The estimation is called an event plane.

3.2 Decomposition of azimuthal part of momentum distribution

The triple differential momentum distribution can be decomposed by using the Fourier transform with the respect to the reaction plane as follows:

$$E\frac{d^3N}{d^3p} = \frac{1}{2\pi}\frac{d^2N}{p_T dp_T dy}\left(1 + \sum_{i=1}^{\infty} 2v_n \cos(n(\phi - \Phi^{RP}))\right),$$

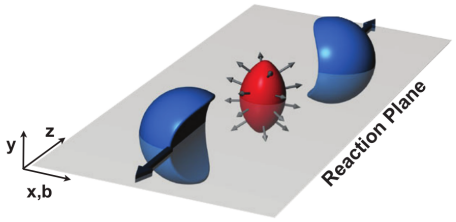

Figure 3.1: Initial geometry of a non-central collision taken from [**31**]. A reaction plane is drawn by grey color.

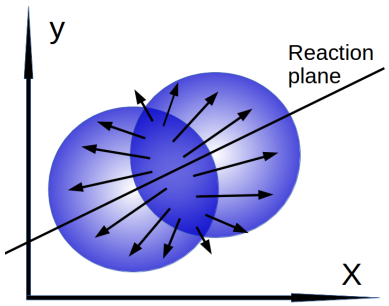

Figure 3.2: Transverse plane of the relativistic heavy ion collision.

where N is number of particles, E energy, y rapidity, v_n n-th Fourier coefficient, ϕ azimuthal angle and Φ^{RP} an azimuthal angle of reaction plane [**27**].

Coefficients v_n can be expressed as

$$v_n = \langle \cos(n(\phi - \Phi^{RP})) \rangle$$

in this formalism. However, it is not so simple to obtain flow coefficients v_n in the case of finite multiplicity. Event planes are not identical with reaction planes and coefficients v_n should be corrected to event-plane resolution as is explained later in the subchapter about event plane method.

Coefficients v_n correspond to the various modifications of the momentum distribution. The flow corresponding to the first Fourier coefficient v_1 is called direct flow, the second Fourier coefficient v_2 is called elliptic flow, third v_3 triangular flow. The distributions corresponding to $1+0.15\cdot\cos\phi$, $1+0.15\cdot\cos 2\phi$ and $1 + 0.15 \cdot \cos 3\phi$ can be seen in the Figure 3.3.

The direct flow coefficient expresses an extent of an overall distribution shift to one side in the transverse plane. The eliptic flow (resp. triangular flow) corresponds to elipse-like distribution (resp. triangular-like distribution) as the name suggests. We are going to discuss the eliptic flow in this research task.

3.3 Eliptic flow of particles containing of light and strange quarks

It was shown that the particles composed of light and strange quarks have the positive value of v_2 for higher p_T. It can be seen in the Figure 3.4. It shows v_2 at mid-rapidity as a function of p_T for $\pi^{\pm}, K^{\pm}, p, \bar{p}, \Lambda, \bar{\Lambda}, \phi, K^0_s, \Xi^-$ and $\bar{\Xi}^+$ in Au+Au minimum bias (0-80%) collisions at $\sqrt{s_{NN}} = 7.7, 11.5, 19.6, 27, 39$ and 62.4GeV recorded at STAR during the Beam Energy Scan program in years 2010 and 2011 at RHIC [**10**]. The event plane method was used for eliptic flow calculation. In addition, the invariant mass method was also used for ϕ mesons.

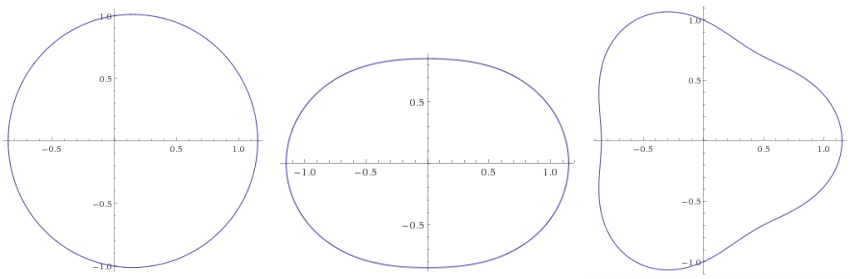

Figure 3.3: The distribution corresponding to direct flow with $v_1 = 0.075$ (the picture on the left), $v_2 = 0.075$ (the picture in the middle) and $v_3 = 00.075$ (on the right). The figures is taken from [**29**].

Results obtained by those technically different methods were identical. Both methods are going to be discussed later in this chapter.

A similar pattern of v_2 was observed for all mentioned particles. v_2 increases with p_T from v_2 close to zero value to the maximum between 0.6 and 2.2. The maximum v_2 increases with the rising beam energy and is smaller for mesons than for hadrons [**10**].

3.4 Eliptic flow of J/ψ

Particles from Figure 3.4 are all composed of light and strange quarks that are deconfined and thermalized in quark-gluon plasma and interact strongly with their surronudings. However, particles such as quarkonia are expected be formed in the early stage of collision before thermalization. They are tightly bound, thus they may survive the whole evolution in the form of colourless mesons. Thus, they should not be thermalized like asymptically free quarks. However, situation is not so simple. Quarkonia can be formed for example also during hadronisation. The quarks of these quarkonia are present in QGP like single quarks and consequently can be easily thermalized. Thus, studying J/ψ eliptic flow can shed more light on the production of J/ψ and interaction of J/ψ with the hot deconfined medium.

3.4.1 J/ψ v_2 in Au+Au collisions at $\sqrt{s_{NN}} = 200$GeV

J/ψ v_2 was analysed in Au+Au collisions at $\sqrt{s_{NN}} = 200$GeV performed at STAR experiment [**10**]. The obtained J/ψ v_2 as a function of p_T can be seen in the upper panel of the Figure 3.5 together with charged hadron and ϕ eliptic flow from the same collisions.

Non-flow estimation is depicted by the green area. There is J/ψ v_2 compared to the various model estimations in the lower pannel of the Figure 3.5.

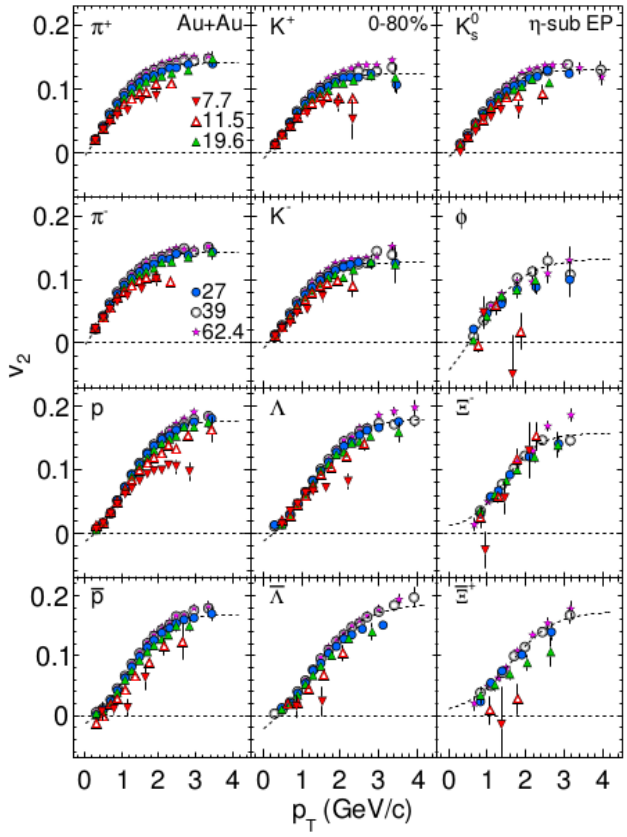

Figure 3.4: v_2 as a function of p_T at mid-rapidity for $pi^{\pm}, K^{\pm}, p, \bar{p}, \Lambda, \bar{\Lambda}, \phi, K^0_s, \Xi^-$ and $\bar{\Xi}^+$ in Au+Au collisions at $\sqrt{s_{NN}}$ = 7.7, 11.5, 19.6, 27, 39 and 62.4GeV. The figure is taken from [**10**].

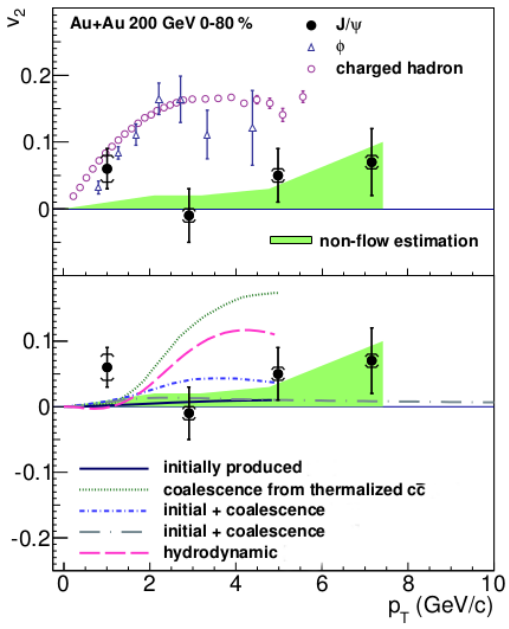

Figure 3.5: J/ψ v_2 for Au+Au collisions at $\sqrt{s_{NN}}$ = 200GeV performed at STAR experiment for p_T bins $0-2$, $2-4$, $4-6$ and $6-10\mathrm{GeVc}^{-1}$. The brackets correspond to systematic errors. The upper panel: J/ψ v_2 together with charged hadron and ϕ v_2 from the same collisions. The lower pannel: J/ψ v_2 compared to the various model estimations. The figure is taken from [**3**].

Eliptic flow of J/ψ was obtained for four p_T bins, namely $0-2$, $2-4$, $4-6$ and $6-10\mathrm{GeVc}^{-1}$, by the event plane method and the invariant mass method. Systematic errors was estimated from differences between v_2 calculated by those methods with three sets of electron/positron cuts.

We can observe that charged hadron and ϕ v_2 are considerably higher than J/ψ v_2. Charged hadron v_2 is close to zero for p_T under $0.5\mathrm{GeVc}^{-1}$. As p_T increases also charged hadron v_2 rises. The maximum eliptic flow value of approximately 0.17 is reached at p_T corresponding to $3\mathrm{GeVc}^{-1}$ in the case of charged hadrons. The ϕ meson v_2 trend is similar to the trend of charged hadrons v_2. However, ϕ meson v_2 acquires slightly smaller values for p_T between 0 and $2\mathrm{GeVc}^{-1}$. v_2 of J/ψ for p_T bin $2-4\mathrm{GeVc}^{-1}$ and bins with higher p_T is small in comparison to charged hadrons and ϕ v_2, moreover it is consistent with zero for mentioned p_T bins. We can also deduce that J/ψ is probably not mostly produced by the coalescence according to the data. Only v_2 of J/psi in first p_T bin is not consistent with zero.

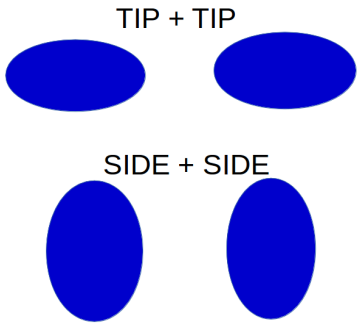

Figure 3.6: Picture of "tip+tip" collision and "side+side" uranium collisions.

3.4.2 J/ψ v_2 in U+U collisions

Uranium nuclei have most nucleons from all ions collidet at RHIC. For exapmle, ions of gold collided at RHIC have 197 nucleons, whereas uranium ions have 238 [**2**]. Thus, greater energy density can be reached in uranium collisions than in gold collisions. Moreover, atoms of gold has spherical shape, whereas uranium nuclei is rather elipsoidal. Thus, uranium collisions are great opportunity to study hot nuclear matter effects at different geometries. Uranium nuclei can be collided for example side to side ot tip to tip as is shown in the Figure 3.6. Energy densities reached in tip to tip collisions are even greater than energy densities that would be present in collisions of spherical nuclei with the same number of nucleons. Thus, extent of thermalization should be the most significant in U+U tip-to-tip collisions. It will be interesting to study properties of hot and dense medium present in U+U collisions also through eliptic flow .

3.5 Standard event plane method

Here we are going to discuss one method that can be used for v_n calculation, the standard event plane method [**26**].

Since the reaction plane is not known, we can only estimate it. The estimation is called the event plane.

At first, we need to calculate the 2-D event flow vector $\vec{Q}_n$ in the transverse plane, which lies in the event plane.

$$Q_{x,n} = \sum_i w_i \cos(n\phi_i) = Q_n \cos(n\Phi_n) \tag{3.1}$$

$$Q_{y,n} = \sum_i w_i \sin(n\phi_i) = Q_n \sin(n\Phi_n) \tag{3.2}$$

i goes ower all particles of event. w_i is the weight for i-th particle. It is common to use transverse momentum p_T as the weight. ϕ_i is the laboratory

angle of the particle flight.

Afterwards, the event plane angle can be calculated as

$$\Phi_n = \left(\tan^{-1} \frac{Q_{x,n}}{Q_{y,n}} \right) / n. \tag{3.3}$$

The observed coeficient can be obtained by formula

$$v_n^{obs}(p_T, y) = \langle \cos[n(\phi_i - \Phi_n)] \rangle \tag{3.4}$$

where $\langle\rangle$ donates the an average over all particles in all events.

We do not have the infinite number of particles, therefore v_n^{obs} have to be corrected by the event plane resolution

$$\mathcal{R}_n = \langle \cos[n(\Phi_n - \Phi_{RP})] \rangle.$$

v_n can be obtained by

$$v_n = \frac{v_n^{obs}}{\mathcal{R}_n}.$$

However, we do not know the reaction plane angle used in the formula for $\mathcal{R}_n$ calculation. Thus, the $\mathcal{R}_n$ can be obtained by following iterative method. We randomly devide the events to two subevents with the same multiplicity and obtain the event plane resolution for these subevents:

$$\mathcal{R}_{n,sub} = \sqrt{\langle \cos[n(\Phi_n^A - \Phi_n^B)] \rangle}.$$

The event plane resolution can be estimated by

$$\mathcal{R}_{n,full}(\chi) = \mathcal{R}(\sqrt{2}\chi_{sub}),$$

where $\chi_{sub} = v_{n,sub}\sqrt{M} = \frac{v_{n,sub}^{obs}}{\mathcal{R}_n^{obs}}\sqrt{M}$. M is a number of particles in a subevent. The first approximation is given by $\mathcal{R}_{full} \approx \sqrt{2}\mathcal{R}_{sub}$. We can further iterate by substituting $\mathcal{R}_{full}$ in $\chi = v_n\sqrt{M}$ and calculation of

$$\mathcal{R}_k(\chi) = \frac{\sqrt{\pi}}{2}\chi \exp\left(\frac{-\chi^2}{2}\right)\left(I_{(k-1)/2}\left(\frac{\chi^2}{2}\right) + I_{(k+1)/2}\left(\frac{\chi^2}{2}\right)\right),$$

where I donates modified Bessel function. This method is taken from [**26**].

The standard event plane method does not take into account that there can be considerable background if we reconstruct particle from the others, for example J/ψ via e^-e^+ decay channel. We are not able to distinguish which exact pairs e^-e^+ originated from J/ψ and which from combinatorial background or Drell-Yan pairs. Thus, it is better to use the modified event plane method or the invariant mass method. Both are going to be described in the following subchapters.

3.6 Modified event plane method

The modified event plane method for v_2 calculation that is not sensitive to flow of background as previously discussed method is going to be discussed in this chapter.

At first, the projections of Q_2-vector are obtained by formulas 3.1 and 3.2 for $n = 2$. The event plane angle Φ_2 is calculated according to equation 3.3 for $n = 2$. Tracks that are going to be used for reconstruction of signal used for v_2 calculation are needed to be removed from tracks used for obtaining Φ_2 to avoid autocorrelation. The event plane resolution is obtained by the procedure described in previous subchapter.

Subsequently, the signal of particles is reconstructed for $\phi - \Phi_2$ bin and chosen p_T bin, for example the signal of J/ψ from dielectron decay channel. The background is subtracted bin by bin in $(\phi - \Phi_2)$-distribution or the fitting function of the background is subtracted from the fit function of the signal peak. Yields in each $\phi - \Phi_2$ bin are obtained by integrating. The yield $dN/d(\phi - \Phi_2)$ as a function of $\phi - \Phi_2$ is fitted by

$$A[1 + 2v_2^{obs} \cos(2(\phi - \Phi_2))]. \tag{3.5}$$

This part of the method can be seen in the Figure 3.7. There is the yield $1/N \cdot dN/d(\phi - \Phi_2)$ of ϕ mesons as a function of $\phi - \Phi_2$ from Au+Au collisions at $\sqrt{s_{NN}} = 39$GeV in the transverse momentum range $0.8 < p_T < 1.0\text{GeVc}^{-1}$.

Finally, v_2^{obs} is corrected on the event plane resolution.

3.7 Invariant mass method

This method was firstly proposed in [**32**].

The event plane angle and event plane resolution are obtained by the procedure described in the second paragraph of the previous subchapter. Afterwards, invariant mass distribution is obtained for certain p_T bin. The equation 3.4 is used for v_2^{obs} extraction in each invariant mass bin and $v_2^{obs}(M_{inv})$ is corrected on the event plane resolution. The overall $v_2^{S+B}(M_{inv})$ of the signal and the background as the function of the invariant mass M_{inv} is obtained.

The number of background pairs $N_B(M_{inv})$ and the number of signal pairs $N_S M_{inv}$ as the function of invariant mass M_{inv} is obtained, for exapmle by fitting the invariant mass distribution of like-sign and unlike-sign pairs in the case of J/ψ. Since, the number of signal and background pairs $N_{S+B}(M_{inv})$ is equal to $N_S(M_{inv}) + N_B(M_{inv})$, we can write

$$N_{S+B}(M_{inv})v_2^{S+B}(M_{inv}) = N_S(M_{inv})v_2^S + N_B(M_{inv})v_2^B(M_{inv}), \tag{3.6}$$

which leads to [**27**]

$$v_2^{S+B}(M_{inv}) = \frac{N_S(M_{inv})}{N_{S+B}(M_{inv})}v_2^S + \frac{N_B(M_{inv})}{N_{S+B}(M_{inv})}v_2^B(M_{inv}). \tag{3.7}$$

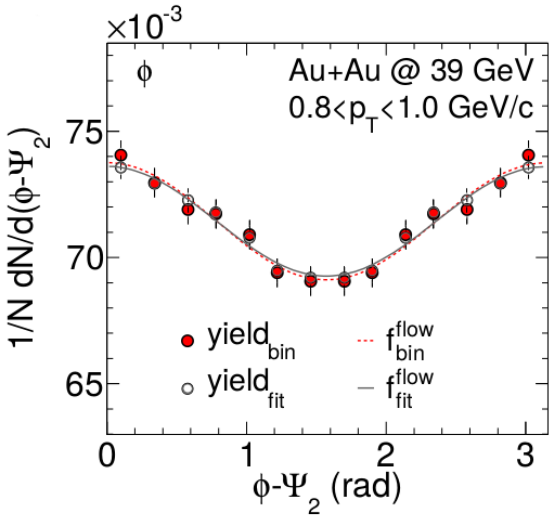

Figure 3.7: Normalized yield $1/N \cdot dN/d(\phi - \Phi_2)$ of ϕ mesons as a function of $\phi - \Phi_2$ from Au+Au collisions at $\sqrt{s_{NN}} = 39$GeV in the transverse momentum range $0.8 < p_T < 1.0\text{GeVc}^{-1}$. Data are marked by red circles, their fit by the function 3.5 is shown as solid black line. Yield points corresponding to the fit are white. The figure is taken from [**10**].

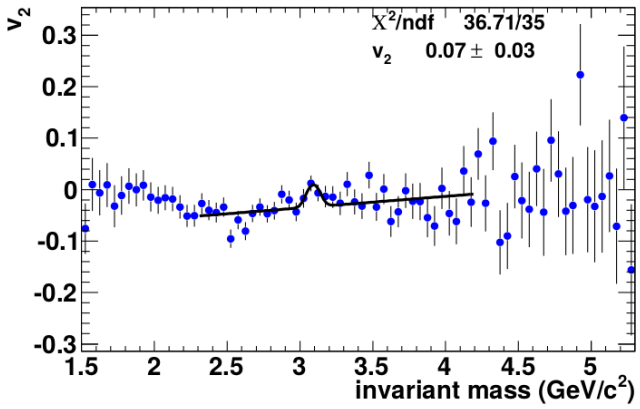

Figure 3.8: $v_2^{S+B}(M_{inv})$ of J/ψ for $0 < p_T < 2\text{GeVc}^{-1}$ in Au+Au collisions with centrality $0 - 80\%$ and its fit. The figure is taken from [**33**].

Finally, if $v_2^{S+B}(M_{inv})$, $N_{S+B}(M_{inv})$, $N_S(M_{inv})$ and $N_B(M_{inv})$ are known, we are able to fit $v_2^{S+B}(M_{inv})$ by the function 3.7. However, there is assumption on the function $v_2^B(M_{inv})$ needed. $v_2^B(M_{inv})$ is often taken as linear function of M_{inv} for the example.

The method is illustrated in the Figure 3.8, where $v_2^{S+B}(M_{inv})$ of J/ψ for $0 < p_T < 2\text{GeVc}^{-1}$ in Au+Au collisions with centrality $0 - 80\%$ and its fit is shown.

Chapter 4

Data analysis

This chapter is dedicated to the analysis of the real data. Firstly, recentering and eventplane azimuthal angle calculation are described. Afterwards, electron and positron preselection is discussed. Finally, J/ψ signal from events triggered as central, minimum bias or with hit in high tower was reconstructed.

4.1 Recentering

The distribution of azimuthal event-plane angle Φ_2 for a big data sample should be uniform. However, an efficiency of detectors, and between them also the efficiency of TPC that is used for event-plane angle calculation, is angle-dependent. Thus, recentering is needed to be done to correct influence azimuthally non uniform TPC efficiency.

4.1.1 Theoretical description of recentering

Flow vectors for second harmonics are calculated for every day and multiplicity by following formulas:

$$Q_{x,2,d,c} = \sum_{i=1}^{N_{d,c}} w_i \cos(2\phi_i),$$

$$Q_{y,2,d,c} = \sum_{i=1}^{N_{d,c}} w_i \sin(2\phi_i),$$

where $Q_{x,2,d,c}$ is a x-projection of $Q_{2,d,c}$-vector counted from tracs from one day and centrality and $Q_{y,2,d,c}$ its y-projection. ϕ_i is the a laboratory angle of a particle flight. A particle transverse momentum p_T is taken as a weight w_i. i goes over particles satisfying track cuts discussed later from events with certain centrality recorded in definite one day. $N_{d,c}$ is number of these events.

Afterwards, the average magnitude of Q-vector x- and y-projection per one track are obtained by

$$\bar{Q}_{x,2,d,c} = \frac{Q_{x,2,d,c}}{N_{d,c}}, \bar{Q}_{y,2,d,c} = \frac{Q_{y,2,d,c}}{N_{d,c}}.$$

$\bar{Q}_{2,d,c}$-vector with projections $\bar{Q}_{x,2,d,c}$ and $Q_{y,2,d,c}$ is subtracted from single-particle Q-vector for more precise event-plane angle reconstruction. Q-vector of event plane can be obtained by formula

$$Q_{x,2} = \sum_{i=1}^{N_{ev}} (w_i \cos(2\phi_i) - \bar{Q}_{x,2,d,c}), \tag{4.1}$$

$$Q_{y,2} = \sum_{i=1}^{N_{ev}} (w_i \sin(2\phi_i) - \bar{Q}_{y,2,d,c}), \tag{4.2}$$

where ev marks that the sum goes over single event. The formula for event-plane angle Φ_2 calculation is following:

$$\Phi_2 = \left(\tan^{-1} \frac{Q_{x,2}}{Q_{y,2}} \right) /2.$$

4.1.2 Recentering of real event planes

The minimum bias data were used for recentering method, namely those marked as vpd-zdc-mb (400004, 400014) and vpd-zdc-mb-protected (400005, 400015, 400025, 400035). Code for recentering was run on MuDST files.

Events without primary vertex or with negative multiplicity was skipped. An event cut for z-vertex position was applied to choose only events with z-position close to the center of the detector:

- $|v_z| < 30$cm.

Distribution of the primary vertex position after cut can be seen in the Figure 4.2. Multiplicity of chosen events is shown in the Figure 4.3. Centrality of event was selected on the base of an event multiplicity. Multiplicity boundaries used in centrality definition are based on Matsui's work [**30**] and can be seen in the Table 4.1. Centralities of events used for recentering are shown in the Figure 4.3.

Following track cuts were applied after the selection of events:

- $|charge| = 1$,
- $15 < nHitsFit$,
- $0.52 < nHitsRatio$,
- global $DCA < 2$cm,

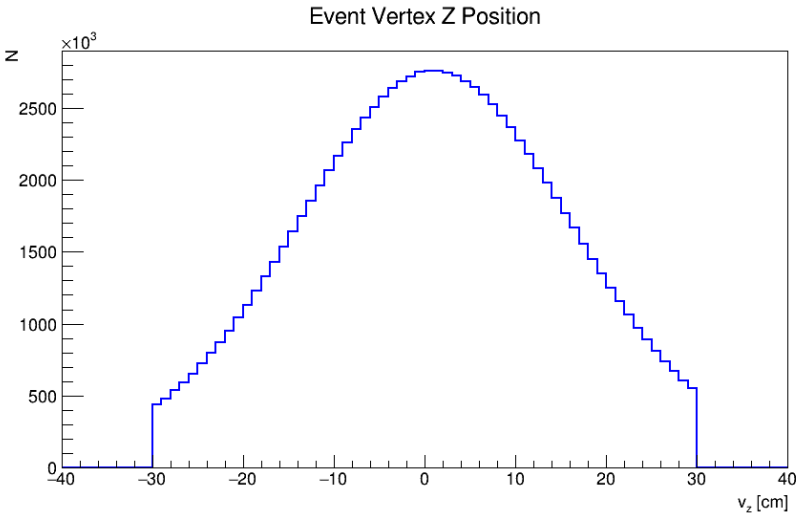

Figure 4.1: Distribution of primary vertex z-position of minimum bias events used for recentering after cut $|v_z| < 30$cm.

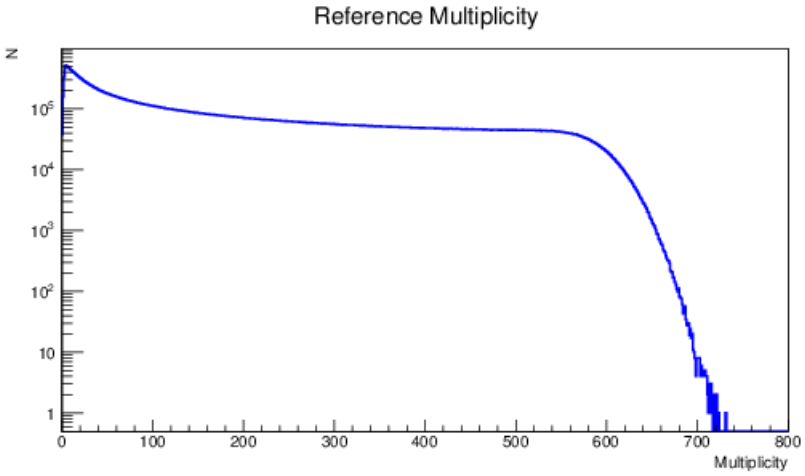

Figure 4.2: Distribution of multiplicity of minimum bias events with $|v_z| < 30$cm used for recentering.

Centrality	Multiplicity
10 %	> 466
20 %	> 339
30 %	> 233
40 %	> 151
50 %	> 91
60 %	> 50
70 %	> 24
80 %	> 10
90 %	> 4

Table 4.1: The definition of centralities based on Monte Carlo Glauber Model and Matsui's work are taken from [**30**].

- $0.15 < p_T < 2$GeV,
- $|\eta| < 1$.

Only particles with charge equal to 1 or -1 were used for the recentering. The minimum demanded number of fitted hits in TPC $nHitsFit$ was 16. The cut $0.52 < nHitsRatio$ on a ratio of fitted hits to number of hits that a particle could leave in TPC was utilized. This cut is applied to avoid usage of two tracks arising from fitting hits that one particle left in TPC. Only primary tracks with a global $DCA < 2$cm were used for the recentering. Additionally, only particles satisfying cuts on a transverse momentum $0.15 < p_T < 2$GeV and a presudorapidity $|\eta| < 1$. was chosen.

The distribution of a number of fitted hits in TPC from all events used for the recentering with the cut is shown in the Figure 4.4, the distribution of a ratio of fitted to possible hits in TPC with the applied cut in Figure 4.5, the distribution of a global-track distance of closest approach in the Figure 4.6, the distribution of a particle transverse momentum and pseudorapidity with the applied cuts in the Figures 4.7 and 4.8.

The distribution of an event-plane azimuthal angle from events used for the recentering before the recentering is shown in the Figure 4.9. The distribution is not uniform. This fact confirms that the recentering is needed. $\bar{Q}_{2,d,c}$-vector averaged over all events and tracks in definite day and centrality is stored and later subtracted from Q-vector of each particle as is demonstrated in the equations 4.1 and 4.2.

4.1.3 Recentered eventplanes

The event planes were obtained by the procedure described in the subchapter about the theoretical description of the recentering. Code for recentered eventplane angles calculation was run on MuDST files.

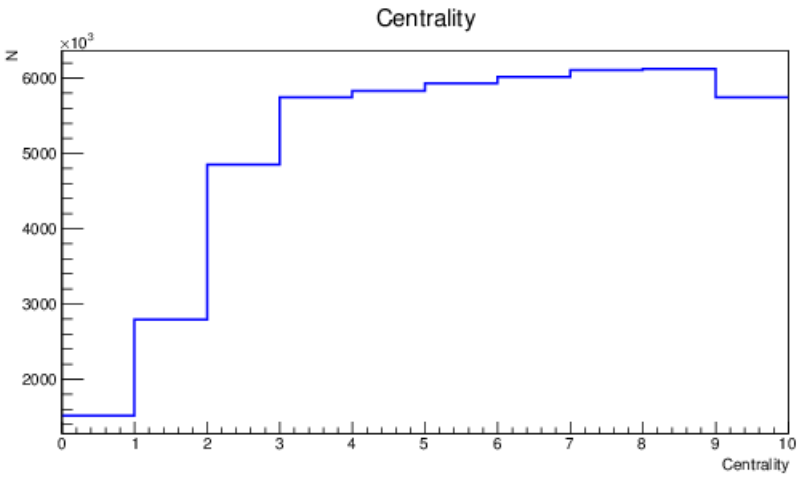

Figure 4.3: Distribution of multiplicity of minimum bias events with $|v_z| < 30$cm used for recentering.

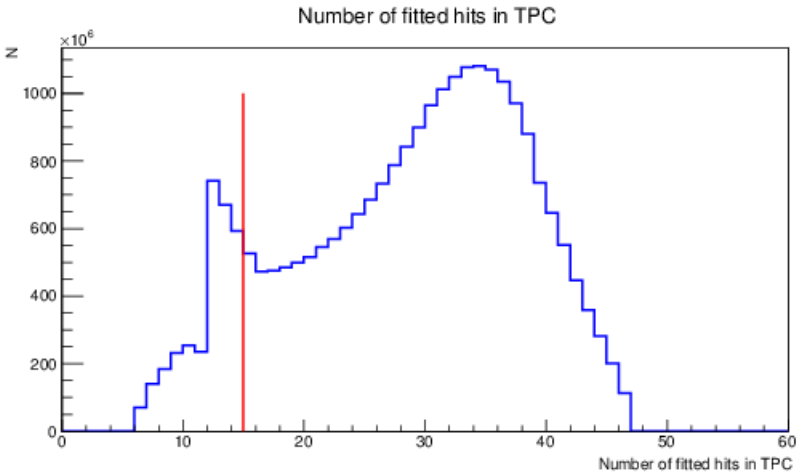

Figure 4.4: Distribution of number of fitted hits in TPC, that was used for track reconstruction. The condition $15 < nHitsFit$ is demanded for tracks used to the recentering.

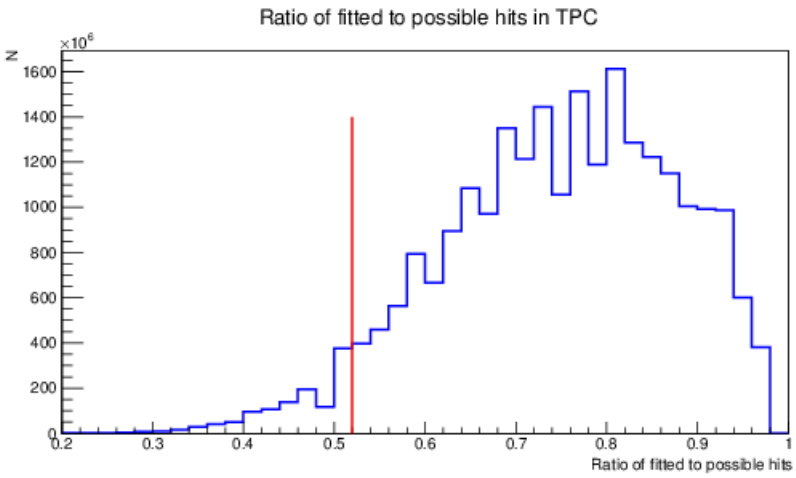

Figure 4.5: Distribution of ratio of fitted to possible hits in TPC. The condition $0.52 < nHitsRatio$ is demanded for tracks used to the recentering.

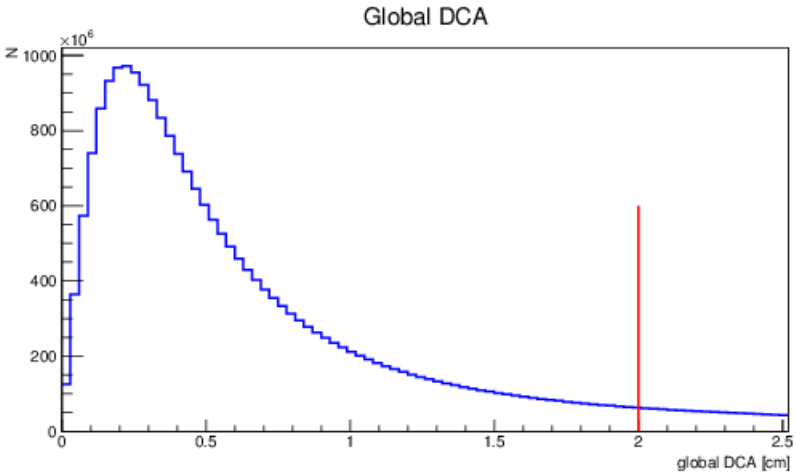

Figure 4.6: Distribution of global-track distance of closest approach. The condition global $DCA < 2$cm is demanded for tracks used to the recentering.

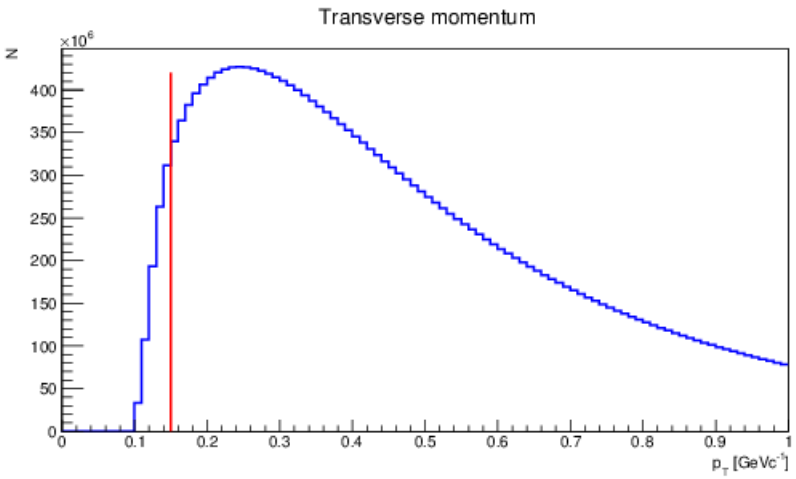

Figure 4.7: Distribution of particle transverse momentum. The condition $0.15 < p_T < 2\text{GeV}$ is demanded for tracks used to the recentering.

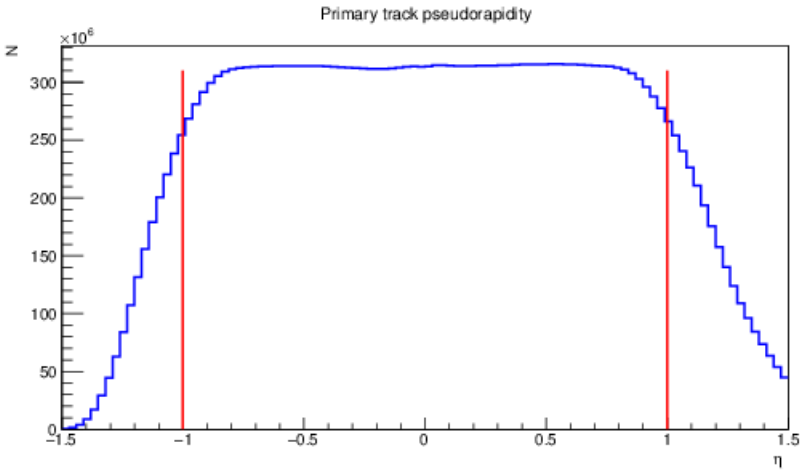

Figure 4.8: Distribution of particle momentum. The condition $|\eta| < 1$ is demanded for tracks used to the recentering.

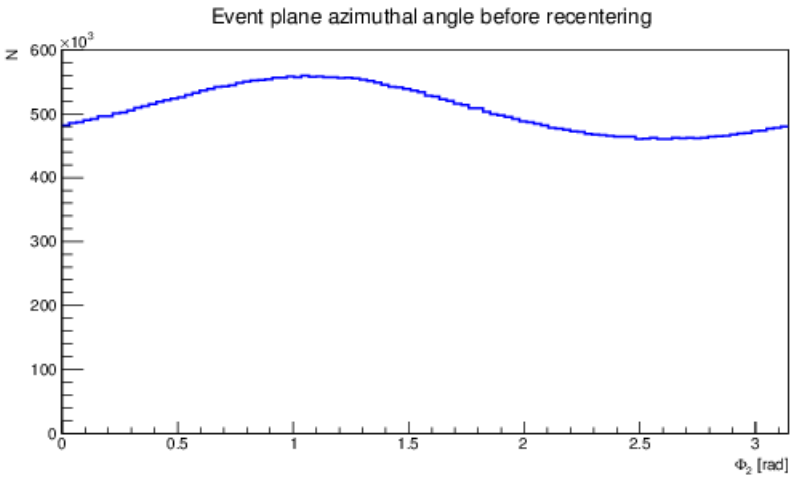

Figure 4.9: The distribution of an event-plane azimuthal angle of events used for the recentering before the recentering.

Events with following triggers were used for event plane angle calculation: central_5 (400101,400121,400111, 400122, 400132, 400142, 400102), central_1 (400103, 400113, 400109, 400119), NPE_11 (400201, 400211), NPE_15 (400202, 400212), NPE_18 (400203, 400213), NPE_25 (400204, 400214), NPE_25_ozdc (400205, 400215), TOF_Mult (400802, 400812), Hadronic (400006, 400016), vpd-zdc-mb (400004, 400014), vpd-zdc-mb-protected (400005, 400025, 400035), zdc-bodytip-east (400117, 400127), zdc-bodytip-west (400116, 400126). Espetially minimum bias (vpd-zdc-mb, vpd-zdc-mb-protected), central and high tower triggers (NPE) are important. Minimum bias events provide good data sample for all centralities. Events chosen by high tower triggers contain high-p_T electrons and it is probable that this electron originated from J/ψ decay.

The same event and track cuts as for the recentering were used for the event plane calculation:

- $|v_z| < 30$cm

and

- $|charge| = 1$,
- $15 < nHitsFit$,
- $0.52 < nHitsRatio$,
- global $DCA < 2$cm,
- $0.15 < p_T < 2$GeV,

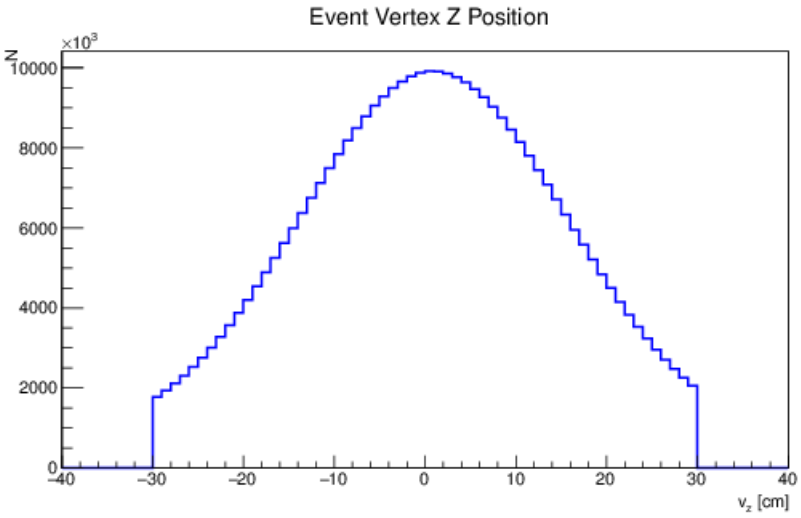

Figure 4.10: Distribution of primary vertex z-position of events used for the event plane reconstruction after cut $|v_z| < 30$cm.

- $|\eta| < 1$.

Distribution of the primary vertex position after cut can be seen in the Figure 4.10. Multiplicity is shown in the Figure 4.11, centrality of events in the Figure 4.12.

The distribution of a number of fitted hits in TPC with the cut can be seen in the Figure 4.13, the distribution of a ratio of fitted to possible hits in TPC together with the cut in the Figure 4.14, the pseudorapidity distribution with the applied cuts in the Figure 4.15.

The distribution of an event-plane azimuthal angle from events used for the recentering before the recentering is shown in the Figure 4.9. The distribution is not uniform. This fact confirms that the recentering is needed. $\bar{Q}_{2,d,c}$-vector averaged over all events and tracks in definite day and centrality is stored and later subtracted from Q-vector of each particle as is demonstrated in the equations 4.1 and 4.2.

The event plane angle Φ_2 distribution after the recentering of all events that passed event cuts is shown in the Figure 4.16. The distribution is almost uniform. If we compare the Figure 4.16 and the Figure 4.9 with the event plane angle distribution of minimum bias events before the recentering, it is obvious that the recentering was useful.

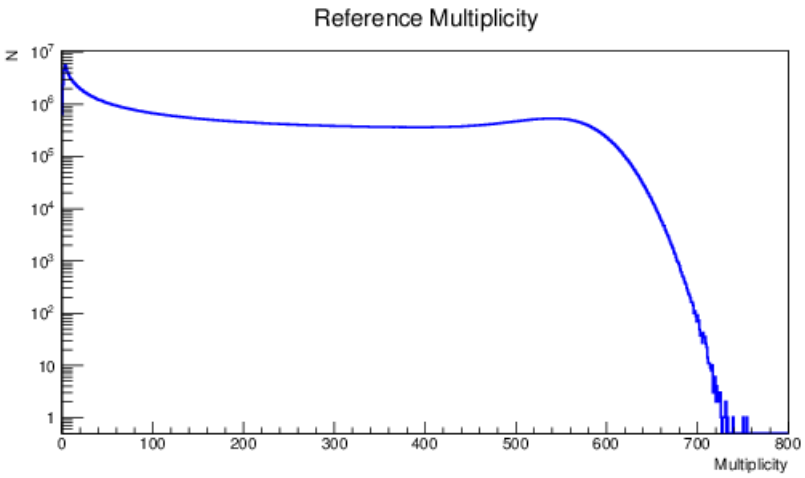

Figure 4.11: Distribution of multiplicity events with $|v_z| < 30$cm used for the event plane reconstruction..

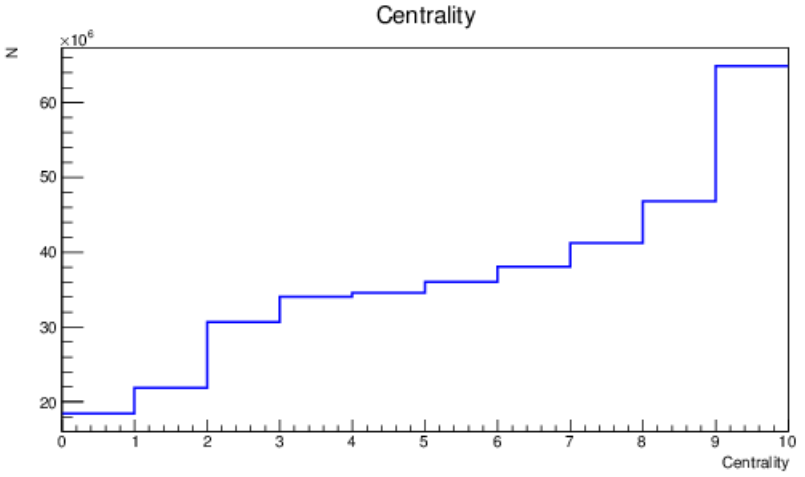

Figure 4.12: Distribution of multiplicity of minimum bias events with $|v_z| <$ 30cm used for the event plane reconstruction.

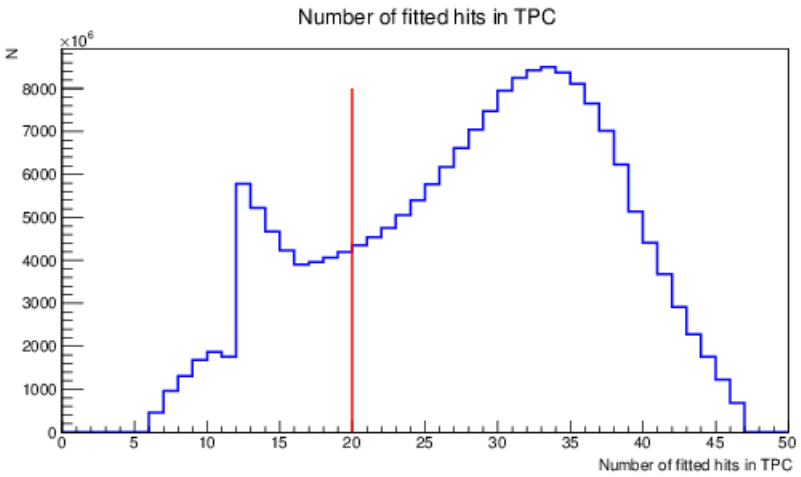

Figure 4.13: Distribution of number of fitted hits in TPC, that was used for track reconstruction of tracks used for the event plane reconstruction. The condition $15 < nHitsFit$ is demanded.

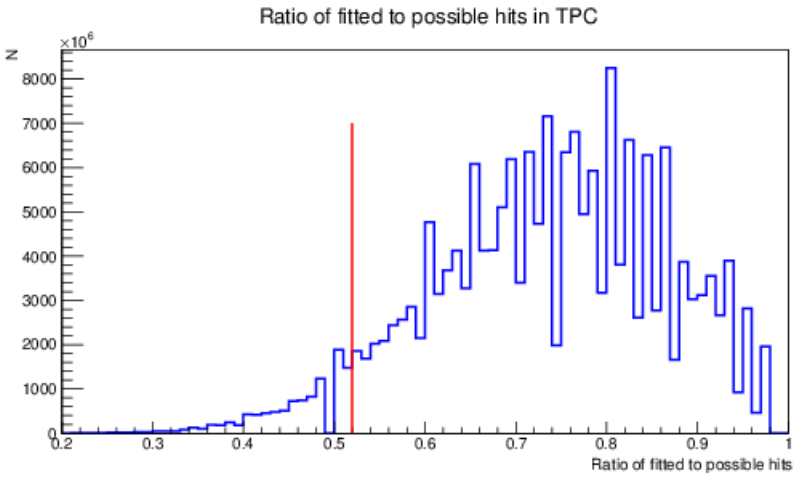

Figure 4.14: Distribution of ratio of fitted to possible hits in TPC of tracks used for the event plane reconstruction. The condition $0.52 < nHitsRatio$ is demanded.

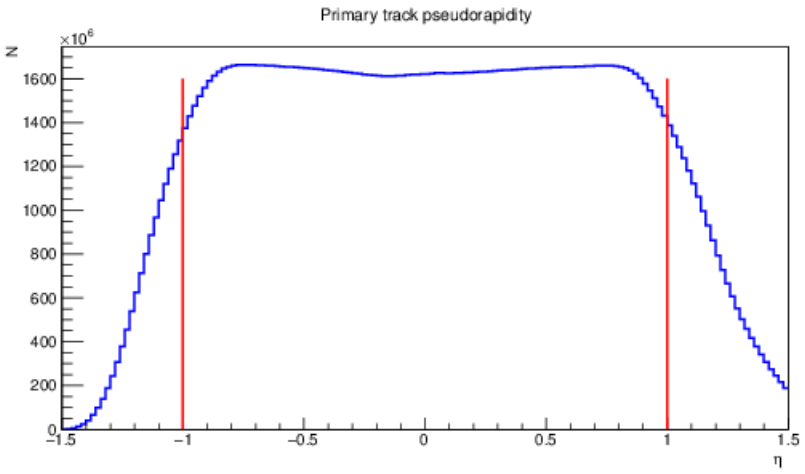

Figure 4.15: Distribution of momentum of tracks used for the event plane reconstruction. The condition $|\eta| < 1$ is demanded for tracks.

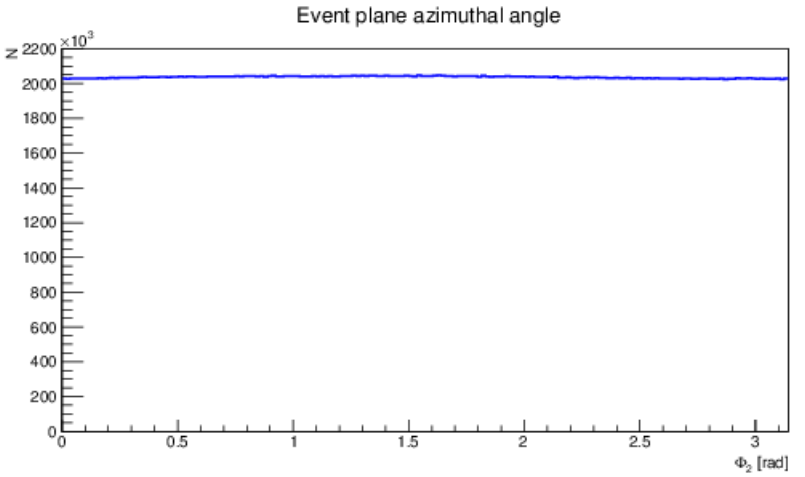

Figure 4.16: The distribution of an event plane azimuthal angle after the recentering.

4.2 Electron and positron preselection

At first, not strict cuts are used for electron and positron preselection by the code running on MuDst. Afterwards, invariant mass of e^+e^-, e^+e^+ and e^-e^- pairs is calculated and informations about them are stored in files called PicoDst.

J/ψ signal can be extracted by applying stricted cuts on unlike-sign pairs, corresponding background by applying same cuts on same-sign pairs. The mechanism of the electron and positron preselection is going to be described in this subchapter, the extraction of J/ψ in following subchapter.

4.2.1 Track cuts demanded on electrons and positrons

Initially, events are preselected for the eventplane calculation as was explained in the previous subchapter. Electrons and positrons are preselected from these events. Follwing track cuts are used for electron and positron candidates:

- $|charge| = 1$,
- $nHitsFit > 20$,
- $nHitsDedx > 15$,
- $nHitsRatio > 0.52$,
- global $DCA < 1$cm,
- $0.3\text{GeVc}^{-1} < p$.

The cuts on $nHitsFit$ and global DCA are stricter than for tracks used for the event plane calculation, since better quality for electron and positron preselection is demanded. Distribution of global DCA of tracks used for the electron and positron preselection after cuts $nHitsFit > 20$, $nHitsDedx > 15$ and $nHitsRatio > 0.52$ is shown in the Figure 4.17. Instead of the cut on particle p_T cut for particle momentum was chosen: $0.3\text{GeVc}^{-1} < p$. Furthermore, the cut on the number of TPC hits used for the energy loss calculation $nHitsDedx$ is applyed.

4.2.2 Electron and positron identification cuts

Few combinations of cuts based on information from TPC, TOF and BEMC were used for distinguishing electrons and positrons from other particles.

- TPC cut: TPC provides information about particle energy loss as was mentioned in the subchapter abou TPC. All particle spacies have their characteristic energy loss dependent on a particle momentum as can be seen in the Figure 2.4. Expected energy loss is described by the Bichsel functions of particle species, for electrons and positrons by dE/dx_e. However, particle energy loss fluctuates around the Bichsel functions. The

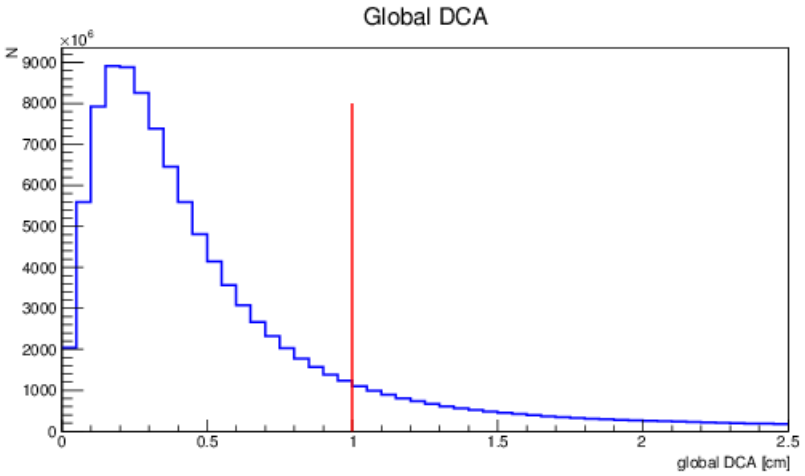

Figure 4.17: Distribution of global track distance of closest approach of tracks used for the electron and positron preselection after following cuts: $nHitsFit > 20$, $nHitsDedx > 15$, $nHitsRatio > 0.52$. The condition of global $DCA < 1$cm is demanded for electron and positron candidates (red line).

extent of fluctuation can be described by quantity $n\sigma$, in case of electrons and positrons $n\sigma_e$:

$$n\sigma_e = ln\left(\frac{dE/dx}{dE/dx_e}\right)/\sigma_{dE/dx},$$

where dE/dx is energy loss of incident particle and $\sigma_{dE/dx}$ its resolution. The $n\sigma_e$ for particles that passed trajectory cuts can be seen in the Figure 4.18. Three combinations of TPC cut with combination of TPC and BEMC cuts were used : $-0.3 < n\sigma_e < 3$, $-2 < n\sigma_e < 3$ and $-3 < n\sigma_e < 3$.

- TOF cut: The electron Bichsel function overlaps with the Bichsel functions of muons and pions approximately at $p \approx 0.15\text{GeVc}^{-1}$ and with the heavier particle Bichsel functions at momenta higher than 0.5GeVc^{-1} as can be seen in the Figure 2.4. TPC cut can be used for better distinguishing between electrons and positrons and other particles. $1/\beta$ of electrons and positrons is approximately equal to 1 for all momenta $p < 0.3\text{GeVc}^{-1}$, whereas $1/\beta$ of heavier particles is considerabely higher for lower momenta and approaches to one for higher momenta. Thus, TOF cut is espetially good for differentiation between particles at low momenta. $1/\beta$ of particles used for electron and positron preselection can be seen in the Figure 4.19 with chosen cut $0.97 < 1/\beta < 1.03$ (black lines). The cut is used in combinations with TPC and BEMC cuts, which are going to be descussed

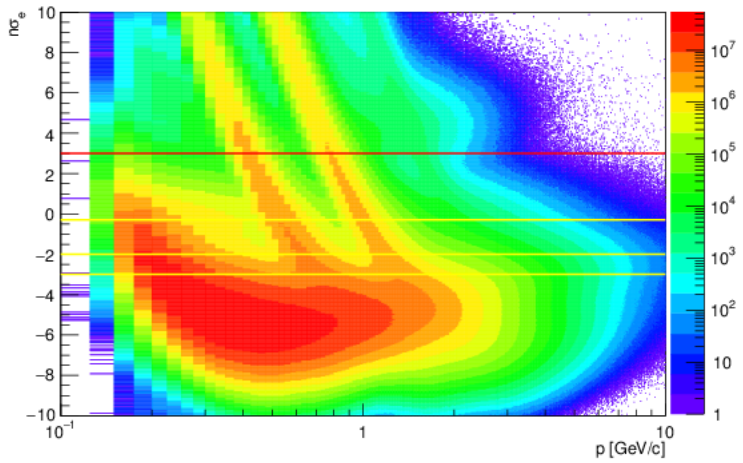

Figure 4.18: $n\sigma_e$ for particles that passed trajectory cuts for electron and positron preselection. Three combinations of TPC cut with combination of TPC and BEMC cuts were used : $-0.3 < n\sigma_e < 3$, $-2 < n\sigma_e < 3$ and $-3 < n\sigma_e < 3$. The upper border of the cuts is shown as the red line, the lower borders as the yellow lines.

later.

- BEMC: Electrons and positrons lose considerable amount of their energy in BEMC in comparison to other particles, in ideal case all its energy is deposited in one tower. pc/E is equal to one in this case. However, one particle can lose its energy in two towers and one tower can be hitted by more particles than one. Following conditions were utilized for the BEMC cut: 0.5GeV$< E$ and $0.3 < pc/E < 1.5$.

Finally, following combinations were used to identify particle as electron or positron:

- $-0.3 < n\sigma_e < 3$ and passing the TOF cut

  or

- $-2 < n\sigma_e < 3$ and passing the EMC cut

  or

- $-3 < n\sigma_e < 3$ and passing the EMC and TOF cuts.

If particle fulfill one of previous combinations, it is preselected as electron or positron. $n\sigma_e$ of particles that passed TOF cut, BEMC cut and both previous cuts are shown in the Figures 4.20, 4.21 and 4.22. Corresponding TPC cuts are

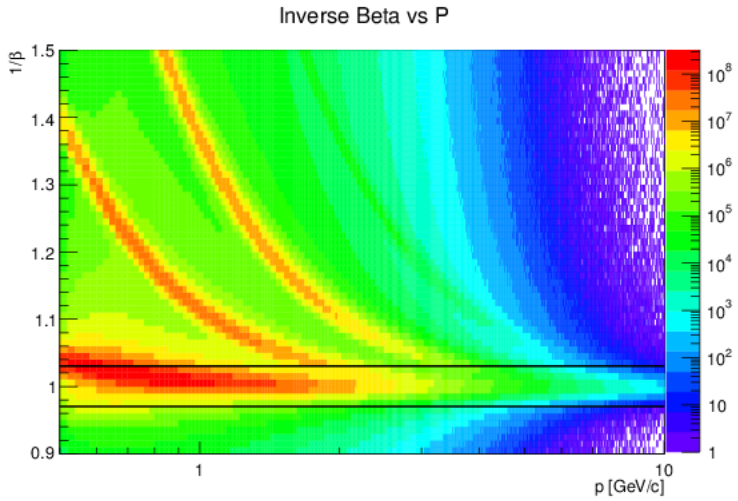

Figure 4.19: $1/\beta$ of particles used for electron and positron preselection after track cuts with the chosen TOF cut: $0.97 < 1/\beta < 1.03$ (black lines).

represented by red lines. Particles between them were preselected as electrons or positrons.

4.3 Reconstruction of J/ψ signal

J/ψ was reconstructed via dielectron decay channel $J/\psi \to e^+e^-$. This channel has branching ratio equal to 5.9 %. Background was obtained by like-sign method. Electrons were combined between themselves and positrons between themselves in the same events.

4.3.1 Saving pairs in PicoDst files

Firstly, following momentum cuts were used for all types of pairs (e^+e^-, e^-e^-, e^+e^+):

- $1.4\text{GeVc}^{-1} < p_1$,
- $1.2\text{GeVc}^{-1} < p_2$,

where p_1 is momentum of faster particle of pair and p_2 momentum of slower. Energy of particles in pair was calculated as follows:

$$E_1 = \sqrt{p_1^2 + m_e^2}, E_2 = \sqrt{p_2^2 + m_e^2},$$

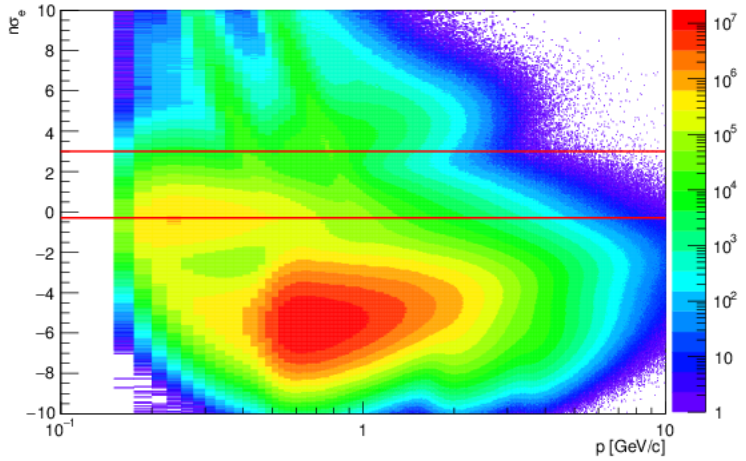

Figure 4.20: $n\sigma_e$ for particles that passed trajectory cuts for electron and positron preselection and the TOF cut. TPC cut $-0.3 < n\sigma_e < 3$ used with TOF cut and without BEMC cut is shown by the red lines. Particles between red lines were preselected as electrons or positrons.

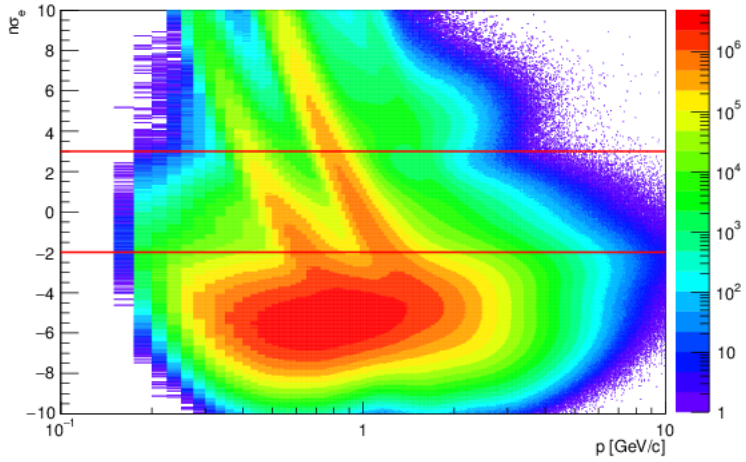

Figure 4.21: $n\sigma_e$ for particles that passed trajectory cuts for electron and positron preselection and the BEMC cut. TPC cut $-2 < n\sigma_e < 3$ used with BEMC cut and without TOF cut is shown by the red lines. Particles between red lines were preselected as electrons or positrons.

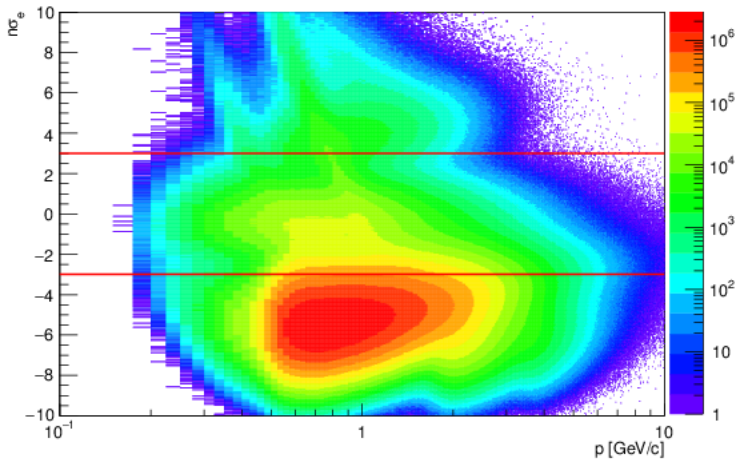

Figure 4.22: $n\sigma_e$ for particles that passed trajectory cuts for electron and positron preselection, BEMC and TOF cut. TPC cut $-3 < n\sigma_e < 3$ used with BEMC and TOF cut is shown by the red lines. Particles between red lines were preselected as electrons or positrons.

where speed of light is taken as equal to 1. Invariant mass of pairs was obtained by formula

$$m = \sqrt{2m_e^2 + 2E_1 \cdot E_2 - 2\vec{p_1} \cdot \vec{p_2}}.$$

Cut on pseudorapidity of pair was applied befor saving pair in PicoDst:

- $y < 1.2$.

Finally, another tighter sets of cuts can be applied on pairs stored in PicoDsts for J/ψ signal reconstruction. One possible set of cuts and corresponding results are shown in next subchapter.

4.3.2 J/ψ signal

The part of code for J/ψ signal reconstruction runs on PicoDsts, where are stored preselected pairs. NPE, minimum bias and central triggers were used for this part of analysis. Tighter cuts were used for extraction of J/ψ signal. These conditions were demanded on electrons and positrons in pairs (p is momentum of electron or positron and E its energy):

- $(-0.6 < n\sigma_e < 3)$ and $(0.3 < pc/E < 1.5)$ and $(1.5\text{GeVc}^{-1} < p)$,
  or

- $(-0.3 < n\sigma_e < 3)$ and $(|1/\beta - 1| < 0.03)$,

  or

- $(-1 < n\sigma_e < 3)$ and $(0.3 < pc/E < 1.5)$ and $(|1/\beta - 1| < 0.03)$.

Other types of cuts (cuts for pairs stored in PicoDsts, cutscuts for electron and positron preselection, trajectory cuts, event cut) that were used and have to be fulfilled are described in previous subchapters.

Significanse of signal was calculated by the formula

$$Sg = \frac{S}{\sqrt{S+B}},$$

where S is number of unlike-sign pairs in the mass region $2.95 < M_{inv} < 3.25\text{GeVc}^{-2}$ and B number of like-sign pairs in the same invariant mass region.

Invariant mass of pairs with all p_T (resp. $0 < p_T < 2\text{GeVc}^{-1}$,$2 < p_T < 5\text{GeVc}^{-1}$, $5 < p_T < 20\text{GeVc}^{-1}$) is shown in the Figure 4.23 (resp. 4.25, 4.27, 4.29). J/ψ signal after background subtraction for all J/ψ p_T (resp. $0 < p_T < 2\text{GeVc}^{-1}$,$2 < p_T < 5\text{GeVc}^{-1}$, $5 < p_T < 20\text{GeVc}^{-1}$) can be seen in the Figure 4.24 (resp. 4.26, 4.28, 4.30). Significance is written under the corresponding Figures.

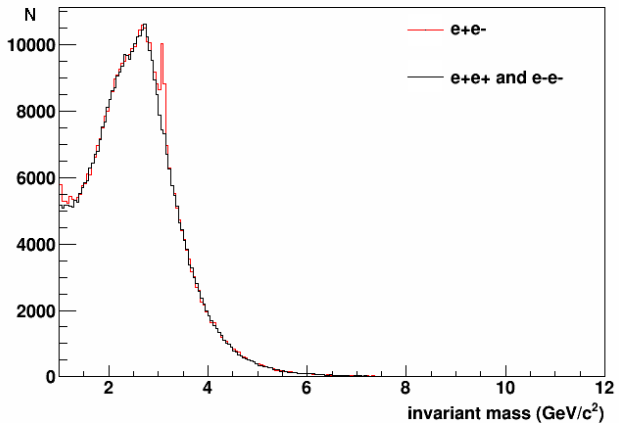

Figure 4.23: Invariant mass distribution of unlike-sign pairs (red line) and like-sign pairs (black line) for all p_T.

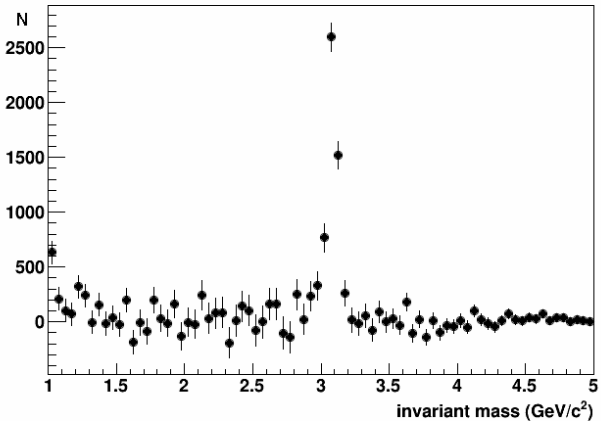

Figure 4.24: Invariant mass distribution after like-sign background subtraction for all p_T of J/ψ. $Sg = 23.2$.

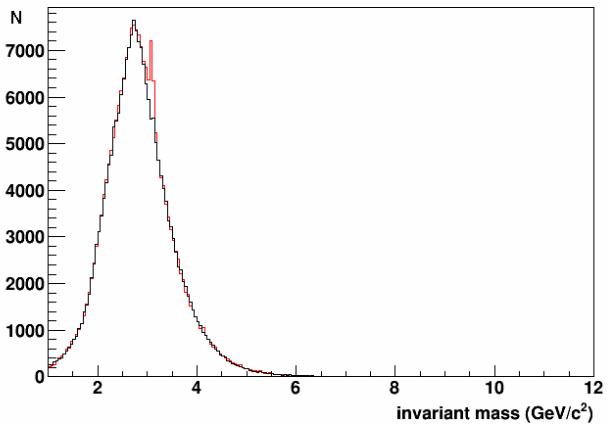

Figure 4.25: Invariant mass distribution of unlike-sign pairs (red line) and like-sign pairs (black line) for $0 < p_T < 2\text{GeVc}^{-1}$.

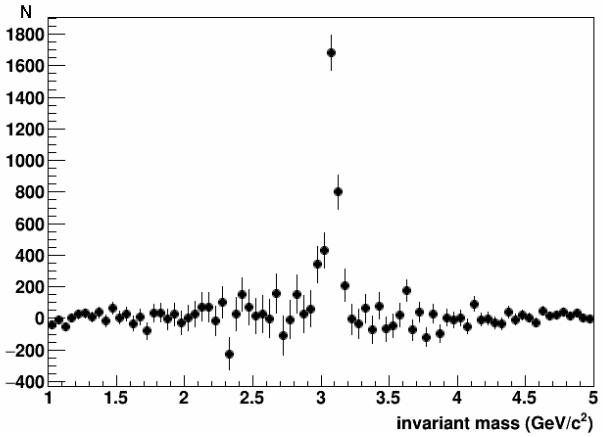

Figure 4.26: Invariant mass distribution after like-sign background subtraction for $0 < p_T < 2\text{GeVc}^{-1}$, where J/psi is transverse momentum of J/ψ. $Sg = 16.9$.

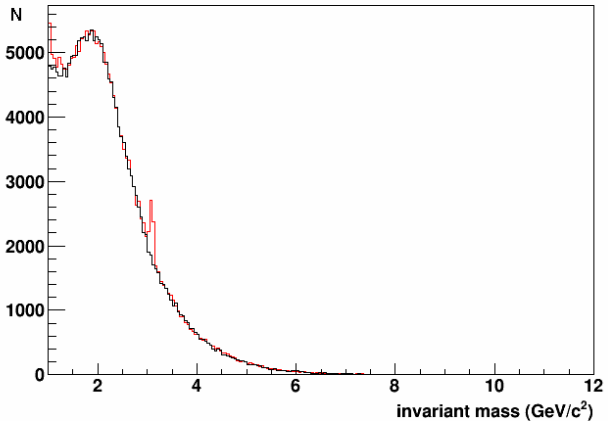

Figure 4.27: Invariant mass distribution of unlike-sign pairs (red line) and like-sign pairs (black line) for $2 < p_T < 5\mathrm{GeVc}^{-1}$.

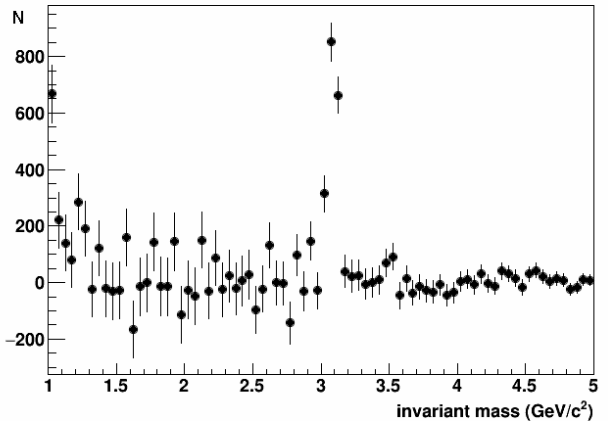

Figure 4.28: Invariant mass distribution after like-sign background subtraction for $2 < p_T < 5\mathrm{GeVc}^{-1}$, where J/psi is transverse momentum of J/ψ. $Sg = 15.8$.

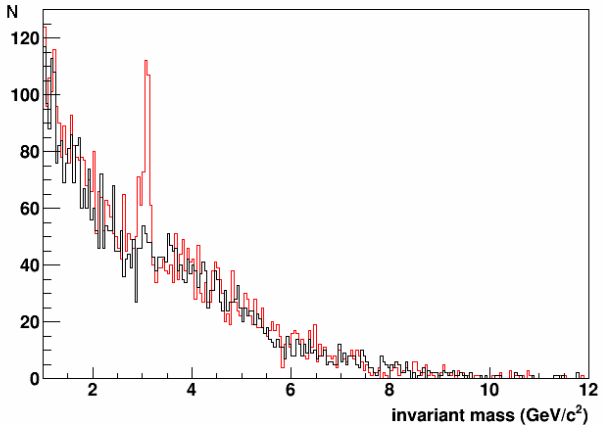

Figure 4.29: Invariant mass distribution of unlike-sign pairs (red line) and like-sign pairs (black line) for $5 < p_T < 20\mathrm{GeVc}^{-1}$.

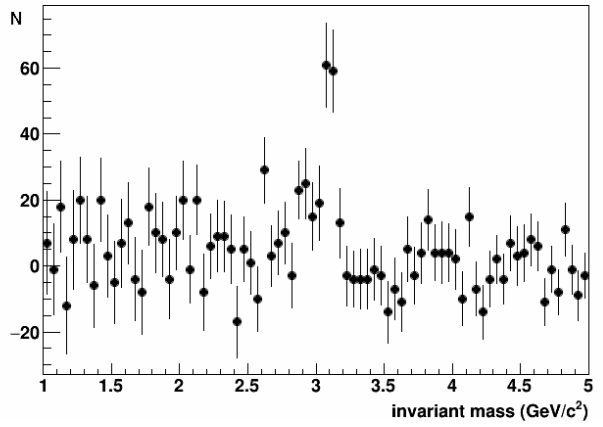

Figure 4.30: Invariant mass distribution after like-sign background subtraction for $5 < p_T < 20\mathrm{GeVc}^{-1}$, where J/psi is transverse momentum of J/ψ. $Sg = 7.2$.

Conclusion and outlook

The goals of this research task were following: 1. Familiarization with physics of ultrarelativistic heavy ion collisions, 2. Studium of problematics of heavy quarkonia production with the focus on the elliptic flow of produced particles, 3. Analysis of data collected in the year 2012 during U+U collisions at $\sqrt{s_{NN}} =$ 200GeV performed at STAR experiment, 4. Analysis of the eliptic flow v_2 of J/ψ meson reconstructed via dielectron decay channel.

Ultrarelativistic heavy ion collisions were discussed in the first chapter. The attention was paid espetially on properties of the strongly interacting matter present in those collisions. Basic information about quark-gluon plasma and possible QCD phase diagram, which are both in the centre of experimental and theoretical interest, was provided.

The importance of the eliptic flow measurement was explained. Part of the STAR results on v_2 calculation was presented. Particles composed of light and strange quarks have considerable positive value of the eliptic flow for higher p_T, whereas v_2 of J/ψ meson in Au+Au collisions is slightly positive and consistent with zero from $p_T = 2\text{GeVc}^{-1}$. Those results shed more light on the origin of J/ψ mesons, they are probably not predominantly produced by coalescence. It would be also interesting to obtain results on J/ψ v_2 in U+U collisions that are expected to have even greater energy density.

STAR experiment, that recorded data from U+U collisions was described in the second chapter. First steps towards reconstruction of v_2 J/ψ in U+U collisions were performed. Event plane azimuthal angles were corrected on TPC efficiency. Electrons and positrons were preselected and unlike-sign and like-sign pairs were saved in PicoDsts. J/ψ signal from events triggered as central, minimum bias or with hit in high tower was reconstructed for following p_T bins: $0 < p_T < 2\text{GeVc}^{-1}$,$2 < p_T < 5\text{GeVc}^{-1}$, $5 < p_T < 20\text{GeVc}^{-1}$.

Further steps of v_2-calculation procedure were discussed in the chapter about the eliptic flow. Modified event plane method and invariant mass method are going to be used for J/ψ v_2 calculation.

Bibliography

[1] "The Physics of RHIC." Brookhaven National Laboratory. Brookhaven National Laboratory. Web. 22 May 2016. **https://www.bnl.gov/rhic/physics.asp**

[2] "Run Overview of the Relativistic Ion Collider." Brookhaven National Laboratory. Brookhaven National Laboratory. Web. 22 May 2016. **http://www.rhichome.bnl.gov/RHIC/Runs/**

[3] "RHIC Complex." Brookhaven National Laboratory. Web. 22 May 2016. **https://www.flickr.com/photos/brookhavenlab/7979381212/in/album-72157613690851651/**

[4] "Star Detector System." STAR. STAR. Web. 22 May 2016. **https://drupal.star.bnl.gov/STAR/book/export/html/7410**

[5] Nu, Xu "An Overview of STAR Experimental Results." ArXiv. Physics (2014): **arXiv:1408.3555v1**

[6] Ackermann, K.H. et al."STAR Detector Overview." Elsevier Science. Physics (2002): **www**

[7] Bergsma, F. et al. "The STAR Detector Magnet Subsystem." Elsevier Preprint. Physics (2002): **www**

[8] Beddo, M.E. et al. "STAR Conceptual Design Report." The STAR Collaboration. Conceptual design Report: **www**

[9] Powell, C.B. "J/ψ Production in Heavy Ion Collisions at the STAR Detector at RHIC." Diss. University of Cape Town, 2012. www

[10] Adamczyk, L. "Elliptic flow of identified hadrons in Au+Au collisions at $\sqrt{s_{NN}} = 7.7$–62.4GeV." ArXiv. Physics (2013): **arXiv:1301.2348v1**

[11] Abelev, B. I. et al. "Hadronic resonance production in d+Au collisions at $\sqrt{s_{NN}} = 200$GeV measured at the BNL Relativistic Heavy Ion Collider." Physics Rewiev C. PHYSICAL REVIEW C 78, 044906 (2008): PHYSICAL REVIEW C 78, 044906 (2008)

[12] Beddo, M. et al. "The STAR Barrel Electromagnetic Calorimeter." Elsevier Science. Physics: **www**

[13] Margetis, Spiros. "STAR Heavy Flavor Tracker." 2014. Presentation.www

[14] Yang, C. "Calibration and performance of the STAR Muon Telescope Detector using cosmic rays." ArXiv. Physics (2014): **arXiv:1402.1078v1**

[15] Chi, Yang. "Performance of the Muon Telescope Detector (MTD2) in STAR at RHIC." 2012. Poster from Quark Matter.**www**

[16] Bieser, F.S. et al."The STAR Trigger." Elsevier Science. Physics (2002): **www**

[17] Adler, C. et al."The RHIC zero degree calorimeters." Elsevier Science. Nuclear Instruments and Methods in Physics Research (2000): **www**

[18] Llope, W.J. et al."The STAR vertex position detector." ArXiv. Physics (2014): **arXiv:1403.6855v1**

[19] M. Kliemant et al., Global Properties of Nucleus-Nucleus Collisions, Lect.Notes Phys. 785 (2010) 23-103

[20] Petracek, V."Subatomová fyzika I." (2009): **www**

[21] Khachatryan, V. et al. "Constraints on parton distribution functions and extraction of the strong coupling constant from the inclusive jet cross section in pp collisions at $\sqrt{s} = 7TeV$". (2014). **ArXiv:1410.6765v2**

[22] Adams, J. et al. "Pion, kaon, proton and anti-proton transverse momentum distributions from p+p and d+Au collisions at $\sqrt{s_{NN}} = 200$GeV". ArXiv. Physics (2005): arXiv:nucl-ex/0309012

[23] Kajimoto, Kohei. "A Large Area Time of Flight Detector for the STAR Experiment at RHIC". Dissertation. (2009): www

[24] Anderson, M. "The STAR Time Projection Chamber: A Unique Tool for Studying High Multiplicity Events at RHIC". ArXiv. (2009): arXiv:nucl-ex/0301015

[25] STAR Collaboration "Studying the Phase Diagram of QCD Matter at RHIC." Presentation. (2014). www

[26] Voloshin,S. A. et al. "Collective phenomena in non-central nuclear collisions." ArXiv. Physics (2008): arXiv:0809.2949

[27] Kikola, D. "Hidden charm production in the relativistic heavy ion collisions registered in the STAR experiment." Ph.D. Thesis. (2010)

[28] Qiu, Hao. "Measurement of J/ψ Azimuthal Anisotropy in Au+Au Collisions at $\sqrt{s_{NN}} = 200$GeV". ArXiv. Nuclear Experiment (2012): arXiv:1212.3304

[29] "$1+2\cdot 0.075\cdot\cos(\phi)$ polar plot, $1+2\cdot 0.075\cdot\cos(2*\phi)$ polar plot and $1+2\cdot 0.075\cdot\cos(3\cdot\phi)$ polar plot." WolframAlpha. 1. Jan. 2016 $1+2\cdot 0.075\cdot\cos(\phi)$ polar plot, $1+2\cdot 0.075\cdot\cos(2*\phi)$ polar plot, $1+2\cdot 0.075\cdot\cos(3\cdot\phi)$ polar plot

[30] H. Matsui, "Preliminary centrality definitions in U+U." Internal STAR presentation, May 2013.

[31] Snellings, R. "Elliptic Flow: A Brief Review", ArXiv. Physics. (2011) arXiv:1102.3010

[32] Borghini, N. "Azimuthally sensitive correlations in nucleus-nucleus collisions." ArXiv. Physics. (2004) arxiv.org/abs/nucl-th/0407041v2

[33] Qiu, H. "J/ψ Azimuthal Anisotropy in Au+Au Collisions at $\sqrt{s_{NN}}$ = 200GeV." Analysis Note. (2012)